Planewave Density Interpolation Methods for the EFIE on Simple and Composite Surfaces

Carlos Pérez-Arancibia, *Member, IEEE*, Catalin Turc, Luiz M. Faria, and Constantine Sideris, *Member, IEEE*

***Abstract*— This article presents an extension of the recently introduced planewave density interpolation method to the electric-field integral equation (EFIE) for problems of scattering and radiation by perfect electric conducting objects. Relying on the Kirchhoff integral formula and local interpolations of the surface currents that regularize the kernel singularities, the technique enables off- and on-surface EFIE operators to be reexpressed in terms of integrands that are globally bounded (or even more regular) over the domain of integration, regardless of the magnitude of the distance between the target and source points. Surface integrals resulting from the application of the method of moments using the Rao–Wilton–Glisson basis functions can then be directly evaluated by means of elementary quadrature rules irrespective of the singularity location. The proposed technique can be applied to simple and composite surfaces comprising two or more overlapping components. The use of composite surfaces can significantly simplify the geometric treatment of complex structures, as the density interpolation method enables the use of separate nonconformal meshes for the discretization of each of the surface components that make up the composite surface. A variety of examples, including multiscale and intricate structures, demonstrate the effectiveness of the proposed methodology.**

***Index Terms*— Composite surfaces, electric-field integral equation (EFIE), electromagnetic scattering, method of moments (MoM), singular integrals.**

I. Introduction

As IS well known, the numerical solution of the classical electric-field integral equation (EFIE) by the method of moments (MoM) (also known as the boundary element method (BEM) in other communities) requires numerical evaluation of (weakly) singular integrals, typically defined over planar triangular surface elements [1]. Several analytical, numerical, and hybrid procedures have been developed over the years to numerically evaluate singular integrals in electromagnetic calculations [2]. The two most well-established approaches to deal with such integrals rely on either the so-called singularity extraction/subtraction technique [3]–[6] or the so-called singularity cancellation technique [7]–[11]. Singularity extraction/subtraction techniques are based on expressing the integrand as the sum of a simple singular term corresponding to static (Laplace) Green functions, whose integral over triangles can be evaluated in closed form, and a smoother (at least bounded) term whose integral can be directly computed by means of standard quadrature rules. On the other hand, singularity cancellation techniques, such as those based on the Duffy transformation [12] and polar change of variables [13], rely on a certain coordinate transformation that effectively cancels the singularity of the kernel, thus producing a nonsingular integral that can be accurately evaluated by means of standard quadrature rules. Recent contributions on this subject include the development of all-analytic techniques [14] that do not rely on numerical integration.

In turn, the off-surface evaluation of the electric field potentials—via which the electromagnetic field is retrieved from the MoM-computed surface current density—involves nonsingular integrals that can in principle be computed by means of standard quadrature rules, provided that the target point is located sufficiently far from the surface charges. However, as the target point approaches the surface, the kernels become nearly singular—a term used to denote functions that possess inordinately large yet not infinite derivatives at a given point. Arguably, a more relevant situation where nearly singular integrals naturally occur is in scattering problems involving two or more obstacles that are very close to each other. Indeed, some of the integrals present in the MoM discretization of the (on-surface) EFIE operator become nearly singular in this case, as integration needs to be performed on one surface with target points placed on another nearby surface. Given that this is a time-honored integration problem within the boundary integral equation community, there are also numerous procedures to tackle it. For instance, a certain generalization of the Duffy transformation for nearly singular integrals was introduced in [15] and [16], and several other techniques in the spirit of the singularity cancellation technique (that can in fact be viewed as some kind of adaptive mesh refinement) can be found in the literature [17]–[22].

This article presents an extension of the planewave density interpolation (PWDI) method—put forth in [23]–[25] for the treatment of weakly singular, hypersingular, and

Manuscript received October 4, 2019; revised March 13, 2020; accepted June 3, 2020. Date of publication July 16, 2020; date of current version January 5, 2021. The work of Carlos Pérez-Arancibia was supported by the Fondo Nacional de Desarrollo Científico y Tecnológico (FONDECYT) under Grant 11181032. The work of Catalin Turc was supported by the NSF under Grant DMS-1614270 and Grant DMS-1908602. The work of Constantine Sideris was supported in part by the NSF under Grant 1849965 and in part by the AFOSR under Grant FA9550-20-1-0087. *(Corresponding author: Carlos Perez-Arancibia.)*

Carlos Pérez-Arancibia is with the Institute for Mathematical and Computational Engineering, Pontificia Universidad Católica de Chile, Santiago 7820436, Chile (e-mail: cperez@mat.uc.cl).

Catalin Turc is with the Department of Mathematical Sciences, New Jersey Institute of Technology, Newark, NJ 07102 USA.

Luiz M. Faria is with INRIA and Laboratoire Poems, ENSTA ParisTech, 91762 Palaiseau Cedex, France.

Constantine Sideris is with the Department of Electrical and Computer Engineering, University of Southern California, Los Angeles, CA 90089 USA.

Color versions of one or more of the figures in this article are available online at https://ieeexplore.ieee.org.

Digital Object Identifier 10.1109/TAP.2020.3008616

nearly singular integrals arising in boundary integral equations formulations of the Laplace and Helmholtz equations—to the EFIE formulation of problems of scattering/radiation by perfect electric conducting (PEC) obstacles represented by simple (either simply or multiply connected) and composite surfaces. Relying on the fact that both on- and off-surface electric field potentials can be recast as vector Helmholtz single-layer operators and potentials, the Helmholtz-PWDI method enables both singular and nearly singular EFIE integrals to be expressed in terms of integrands that are bounded or smoother—depending on the density interpolation order—over the whole surface, independent of the distance between the target and source points. The resulting PWDI-regularized integrals can then be numerically evaluated by means of simple quadrature rules regardless of the location of Green function singularities. It is worth mentioning that given that the proposed kernel-regularization procedure operates at the continuous level, it can be seamlessly used in conjunction with a variety of low- and high-order discretization schemes available in the literature [26]–[29], leading to a significantly simpler treatment of singularities, which ultimately reduces the associated implementation effort. Furthermore, unlike other existing singular integration techniques, the PWDI method has the advantage of being universal, in the sense that the same simple regularization procedure is used to deal with singular and nearly singular integrals at the same time. These properties of the PWDI method make it extremely versatile and easy to incorporate in any type of formulation without requiring any specialized approach-dependent techniques. For the sake of preciseness, in this article, we focus on the classical MoM based on the Rao–Wilton–Glisson (RWG) basis functions for representing closed surfaces with planar triangular meshes.

We take advantage of the capability of PWDI to express on- and off-surface electric field potentials in terms of regular integrands, to extend the EFIE formulation to problems involving PEC obstacles modeled as composite surfaces. Unlike simple surfaces, composite surfaces comprise two or more simply connected overlapping components corresponding to boundaries of subdomains that make up the whole object. The associated integral representation of the electric field based on the multiple-scattering EFIE formulation thus involves surface current densities defined on each of the closed-surface components. Coupled integral equations for those currents are obtained by directly enforcing the PEC boundary condition on both the exterior part, corresponding to the actual boundary of the object, and the interior parts where subdomain boundaries overlap. An immediate consequence of this formulation is that it enables the use of nongeometrically conformal meshes (of the closed-surface components) in the MoM discretization of the resulting integral equation system. This property can significantly simplify the geometric treatment of complex PEC structures consisting of several simpler subparts welded together, as it bypasses the need to construct a good-quality single-domain mesh (which is, in some cases, a time-consuming and tedious task). This property of the multiple-scattering formulation is also particularly attractive at dealing with problems requiring repeated calculations on a surface that is subject to changes in the position of some of its parts, as is the case in some optimal-design problems [30]–[33]. No remeshing and no recomputation of the diagonal block of the impedance matrix are required in this case, by virtue of the translational invariance of the Green's function. This extended multiple-scattering EFIE formulation for composite surfaces shares some similarities with domain decomposition methods based on boundary integral equations [34]–[36]. However, the present approach is simpler both conceptually and computationally, as no direct enforcement of the continuity of surface currents is required wherever two or more closed surfaces overlap. In Section VII-D, we demonstrate the advantages of our composite surface approach by using it to analyze a monopole antenna reflector array, where we are able to obtain a significant saving by reusing the mesh and matrix blocks of a single monopole for all of the elements in the array.

This article is organized as follows. Section II outlines the EFIE formulation for the solution of problem of electromagnetic scattering by PEC obstacles modeled in terms of simple (simply or multiply connected) surfaces. Section III briefly describes the classical MoM discretization of the EFIE. Section IV then introduces the multiple-scattering EFIE formulation for composite surfaces. Closed-form and purely numerical PWDI procedures are presented in Section V. Details of the implementation of the proposed methodology are provided in Section VI. Finally, Section VII presents a variety of numerical examples.

II. Problem Formulation

We start off by presenting the problem of time-harmonic electromagnetic scattering of an incident wave field $(\mathbf{E}^{\text{inc}}, \mathbf{H}^{\text{inc}})$, which illuminates a (possibly multiply connected) bounded PEC object $\Omega \subset \mathbb{R}^3$. The total electromagnetic field $(\mathbf{E}, \mathbf{H})$ satisfies the homogeneous Maxwell's equations

$$\nabla \times \mathbf{E} - ik\mathbf{H} = \mathbf{0} \quad \text{and} \quad \nabla \times \mathbf{H} + ik\mathbf{E} = \mathbf{0} \text{ in } \mathbb{R}^3 \setminus \overline{\Omega} \tag{1}$$

where $k = 2\pi/\lambda = \omega\sqrt{\epsilon\mu}$ is the wavenumber, with λ denoting the wavelength, ω denoting the angular frequency, and $\epsilon > 0$ and $\mu > 0$ denoting the electric permittivity and the magnetic permeability of the medium surrounding Ω, respectively. Expressing the total field in the form $(\mathbf{E}^t, \mathbf{H}^t) = (\mathbf{E}^s, \mathbf{H}^s) + (\mathbf{E}^{\text{inc}}, \mathbf{H}^{\text{inc}})$, we obtain that the scattered field $(\mathbf{E}^s, \mathbf{H}^s)$ satisfies Maxwell's equations (1) together with the boundary condition

$$\hat{\mathbf{n}} \times \mathbf{E}^s = -\hat{\mathbf{n}} \times \mathbf{E}^{\text{inc}} \quad \text{on} \quad \Gamma \tag{2}$$

and the Silver–Müller radiation condition [37]. Per usual, throughout this article, the symbol $\hat{\mathbf{n}}$ denotes the outer unit normal to the surface Γ (in what follows, we focus on the scattering problem only, as the radiation problem is analogous).

The classical EFIE formulation of the scattering problem is derived from an integral representation whereby the scattered electric field is expressed as

$$\mathbf{E}^s(\boldsymbol{r}) = (\mathcal{E}\mathbf{J})(\boldsymbol{r}) := ik(\mathcal{E}_1\mathbf{J})(\boldsymbol{r}) - \frac{1}{ik}(\mathcal{E}_2\mathbf{J})(\boldsymbol{r}) \tag{3}$$

for $\boldsymbol{r} \in \mathbb{R}^3 \setminus \overline{\Omega}$, in terms of the integral operators

$$(\mathcal{E}_1\mathbf{J})(\boldsymbol{r}) := \int_\Gamma G(\boldsymbol{r},\boldsymbol{r}')\mathbf{J}(\boldsymbol{r}')\,\mathrm{d}s' \tag{4a}$$

and

$$(\mathcal{E}_2\mathbf{J})(\boldsymbol{r}) := \nabla \int_\Gamma G(\boldsymbol{r},\boldsymbol{r}')\nabla'_s\cdot\mathbf{J}(\boldsymbol{r}')\,\mathrm{d}s' \tag{4b}$$

where $G(\boldsymbol{r},\boldsymbol{r}') = \mathrm{e}^{ik|\boldsymbol{r}-\boldsymbol{r}'|}/(4\pi|\boldsymbol{r}-\boldsymbol{r}'|)$ is the free-space Green function of the Helmholtz equation and Γ denotes, for the time being, the boundary of Ω. The surface current density $\mathbf{J}$, which is a vector field tangential to the surface, is then the unknown we aim to solve for. Enforcing the PEC boundary condition (2), an integral equation for the unknown surface currents can be found. To this end, the tangential components of (3) are directly evaluated yielding the EFIE

$$\mathsf{E}\mathbf{J} = -\hat{\mathbf{n}}\times\mathbf{E}^{\mathrm{inc}} \quad \text{on} \quad \Gamma \tag{5}$$

for the unknown surface current density $\mathbf{J}$, where $\mathsf{E} = ik\mathsf{E}_1 - (ik)^{-1}\mathsf{E}_2$ is the so-called EFIE operator which is given in terms of

$$(\mathsf{E}_1\mathbf{J})(\boldsymbol{r}) := \hat{\mathbf{n}}(\boldsymbol{r})\times\int_\Gamma G(\boldsymbol{r},\boldsymbol{r}')\mathbf{J}(\boldsymbol{r}')\,\mathrm{d}s' \tag{6a}$$

and

$$(\mathsf{E}_2\mathbf{J})(\boldsymbol{r}) := \hat{\mathbf{n}}(\boldsymbol{r})\times\nabla\int_\Gamma G(\boldsymbol{r},\boldsymbol{r}')\nabla'_s\cdot\mathbf{J}(\boldsymbol{r}')\,\mathrm{d}s'. \tag{6b}$$

III. MoM

Throughout this article, we focus on the classical discretization of the EFIE by means of the MoM using the RWG basis functions [1]. We thus consider a triangulation of the closed surface Γ, which is assumed to be given by the union of N_h planar triangles T_j (i.e., $\Gamma = \bigcup_{j=1}^{N_h} T_j$) with maximum edge size $h > 0$. In order to solve (5), the unknown $\mathbf{J}$ is expanded as

$$\mathbf{J}(\boldsymbol{r}) \approx \sum_{n=1}^{N} I_n\mathbf{f}_n(\boldsymbol{r}), \quad (\boldsymbol{r}\in\Gamma) \tag{7}$$

in terms of the div-conforming RWG basis functions $\mathbf{f}_n$ defined on the N edges of the surface mesh. The expansion coefficients I_n, $1 \le n \le N$, are obtained by substituting the approximation (7) in the integral equation (5), which yields

$$\sum_{n=1}^{N} I_n\mathsf{E}\mathbf{f}_n = -\hat{\mathbf{n}}\times\mathbf{E}^{\mathrm{inc}} \quad \text{on} \quad \Gamma. \tag{8}$$

Testing (8) against the curl-conforming basis functions $\hat{\mathbf{n}}\times\mathbf{f}_n$, $1 \le n \le N$, the following linear system:

$$Z\mathbf{I} = \mathbf{V} \tag{9}$$

is achieved, where the relevant matrices and vectors are $(\mathbf{I})_n = I_n$, $(\mathbf{V})_m = -\langle\hat{\mathbf{n}}\times\mathbf{f}_m, \hat{\mathbf{n}}\times\mathbf{E}^{\mathrm{inc}}\rangle = -\langle\mathbf{f}_m, \mathbf{E}^{\mathrm{inc}}\rangle$ and $Z = ikZ_1 - (ik)^{-1}Z_2$ with $(Z_j)_{m,n} = \langle\hat{\mathbf{n}}\times\mathbf{f}_m, \mathsf{E}_j\mathbf{f}_n\rangle$, $j = 1, 2$. In detail, the entries of impedance matrix components are [38]

$$(Z_1)_{m,n} = \int_\Gamma \mathbf{f}_m(\boldsymbol{r})\cdot\left\{\int_\Gamma G(\boldsymbol{r},\boldsymbol{r}')\mathbf{f}_n(\boldsymbol{r}')\,\mathrm{d}s'\right\}\mathrm{d}s \tag{10a}$$

$$(Z_2)_{m,n} = -\int_\Gamma \nabla_s\cdot\mathbf{f}_m(\boldsymbol{r})\left\{\int_\Gamma G(\boldsymbol{r},\boldsymbol{r}')\nabla'_s\cdot\mathbf{f}_n(\boldsymbol{r}')\,\mathrm{d}s'\right\}\mathrm{d}s \tag{10b}$$

for $1 \le m, n \le N$.

We note here that the kernels in (10a) exhibit only a weak (integrable) $\mathcal{O}(|\boldsymbol{r}-\boldsymbol{r}'|^{-1})$ singularity. The kernels present in (3), on the other hand, are smooth but may become nearly singular as the target point $\boldsymbol{r} \in \mathbb{R}^3 \setminus \overline{\Omega}$ approaches the boundary Γ. A similar phenomenon arises in problems involving two (or more) simply connected domains, say, Ω_1 and Ω_2 with $\Omega = \Omega_1 \cup \Omega_2$ and $\overline{\Omega}_1 \cap \overline{\Omega}_2 = \emptyset$, that are very close to each other (see Fig. 5). Some of the impedance matrix entries (10a) in this case involve outer integrals over $\Gamma_1 = \partial\Omega_1$ and inner integrals over $\Gamma_2 = \partial\Omega_2$, thus leading to nearly singular behavior of the kernel present in the inner integral as the distance $|\boldsymbol{r}-\boldsymbol{r}'|$, with $\boldsymbol{r}\in\Gamma_1$ and $\boldsymbol{r}'\in\Gamma_2$, may become very small but not zero.

IV. Composite Surfaces

We have so far dealt with the case where the PEC object Ω consists of a collection of nonintersecting simply connected domains. Assume now that Ω is a simply connected domain that can be represented naturally as the union of several nonoverlapping subdomains. In order to fix the ideas, let us assume for simplicity that $\Omega = \Omega_1 \cup \Omega_2$ with $\Omega_1 \cap \Omega_2 = \emptyset$, but $\Gamma_1 \cap \Gamma_2 \neq \emptyset$, where $\Gamma_1 = \partial\Omega_1$ and $\Gamma_2 = \partial\Omega_2$, that is, the two domains Ω_1 and Ω_2 share in common a point, a curve, or an open surface (see Figs. 7 and 10).

Instead of using the EFIE formulation posed on the boundary of the obstacle $\partial\Omega$, we prefer to employ an extended multiple-scattering EFIE formulation posed on the composite surface $\Gamma = \Gamma_1 \cup \Gamma_2$ with components Γ_1 and Γ_2. Just as in the simple-surface EFIE formulation presented earlier, we express the scattered field $\mathbf{E}^s$ as (3) in terms of the off-surface operator $\mathcal{E}$ integrating now over $\Gamma = \Gamma_1 \cup \Gamma_2$ and featuring a current density function $\mathbf{J} = [\mathbf{J}_1\ \mathbf{J}_2]^\top$ also defined on Γ. The enforcement of the PEC boundary condition (2) on both Γ_1 and Γ_2 yields the multiple-scattering EFIE

$$\begin{bmatrix}\mathsf{E}_{11} & \mathsf{E}_{12}\\ \mathsf{E}_{21} & \mathsf{E}_{22}\end{bmatrix}\begin{bmatrix}\mathbf{J}_1\\ \mathbf{J}_2\end{bmatrix} = -\begin{bmatrix}\hat{\mathbf{n}}_1\times\mathbf{E}_1^{\mathrm{inc}}\\ \hat{\mathbf{n}}_2\times\mathbf{E}_2^{\mathrm{inc}}\end{bmatrix} \quad \text{on} \quad \Gamma = \Gamma_1\cup\Gamma_2. \tag{11}$$

In (11), the electric field operators $\mathsf{E}_{j\ell}$ are defined just as in (6b) with $\boldsymbol{r}\in\Gamma_j$ and the domain of integration Γ_ℓ, where $\{j,\ell\} = \{1,2\}$.

It should be noted that the system (11) may become singular in the case where two composite objects share one or more edges due to repeated collocated unknowns. This can either be resolved by judicious removal of each set of repeated unknowns or more easily by adjusting the meshing of the surfaces such that no shared edges occur in the final composite system containing all of the objects.

The main advantage of the multiple-scattering EFIE formulation (11) is that it is amenable to MoM discretizations using separate triangular meshes on Γ_1 and, respectively, on Γ_2 that do not conform on $\Gamma_1 \cap \Gamma_2$. Their MoM discretization leads to linear systems similar to (9), whose submatrices Z_1 and Z_2 have entries defined in (10a) and (10b), respectively. It is worth noting here that the MoM discretization of the EFIE formulation (11) gives rise to additional integration challenges not present in the classical EFIE formulation. Indeed, the MoM discretization of the composite surface EFIE formulation (11)

requires numerical evaluation of nearly singular integrals of the form

$$\int_{\Gamma_j} G(\boldsymbol{r},\boldsymbol{r}')\mathbf{f}_n(\boldsymbol{r}')\,\mathrm{d}s' \quad \text{and} \quad \int_{\Gamma_j} G(\boldsymbol{r},\boldsymbol{r}')\nabla'_s\cdot\mathbf{f}_n(\boldsymbol{r}')\,\mathrm{d}s' \tag{12}$$

at target points $\boldsymbol{r}\in\Gamma_i\cap\Gamma_j$, $i\neq j$, using meshes on Γ_i and Γ_j that may not conform to each other on $\Gamma_1\cap\Gamma_2$. We address this as well as other integration issues in Section V, where we show that all the singular and nearly singular kernels arising in EFIE formulations on simple and composite surfaces can be regularized using the PWDI method [24], thus enabling the use of elementary quadrature rules in the practical implementation of the MoM.

V. Planewave Density Interpolation

This section is devoted to the presentation of the PWDI method for the regularization of the kernels associated with the integral operators in (4) and (6b) discretized using RWG basis functions.

Throughout this section, we make use of the Helmholtz single- and double-layer potentials defined, respectively, as

$$(\mathcal{S}\varphi)(\boldsymbol{r}) := \int_\Gamma G(\boldsymbol{r},\boldsymbol{r}')\varphi(\boldsymbol{r}')\,\mathrm{d}s \tag{13a}$$

and

$$(\mathcal{D}\varphi)(\boldsymbol{r}) := \int_\Gamma \frac{\partial G(\boldsymbol{r},\boldsymbol{r}')}{\partial\hat{\mathbf{n}}'}\varphi(\boldsymbol{r}')\,\mathrm{d}s', \quad \boldsymbol{r}\in\mathbb{R}^3\setminus\Gamma \tag{13b}$$

as well as the associated single- and double-layer operators, defined as

$$(\mathsf{S}\varphi)(\boldsymbol{r}) := \int_\Gamma G(\boldsymbol{r},\boldsymbol{r}')\varphi(\boldsymbol{r}')\,\mathrm{d}s \tag{14a}$$

and

$$(\mathsf{K}\varphi)(\boldsymbol{r}) := \int_\Gamma \frac{\partial G(\boldsymbol{r},\boldsymbol{r}')}{\partial\hat{\mathbf{n}}'}\varphi(\boldsymbol{r}')\,\mathrm{d}s', \quad \boldsymbol{r}\in\Gamma \tag{14b}$$

respectively. We recall here that potentials and operators are connected by means of the jump relations [37]

$$\lim_{\delta\to0^+}(\mathcal{S}\varphi)(\boldsymbol{r}\pm\delta\hat{\mathbf{n}}) = (\mathsf{S}\varphi)(\boldsymbol{r}) \tag{15a}$$

and

$$\lim_{\delta\to0^+}(\mathcal{D}\varphi)(\boldsymbol{r}\pm\delta\hat{\mathbf{n}}) = \pm\frac{\varphi(\boldsymbol{r})}{2} + (\mathsf{K}\varphi)(\boldsymbol{r}), \quad (\boldsymbol{r}\in\Gamma) \tag{15b}$$

which hold almost everywhere.

The proposed regularization technique relies on two simple observations.

1) The off-surface EFIE operator $\mathcal{E}$ can be expressed in terms of a vectorial single-layer potential—referred to as $\mathcal{E}_1$ in (4a)—and the gradient of a scalar single-layer potential—referred to as $\mathcal{E}_2$ in (4b).
2) The MoM discretization of the on-surface EFIE operator E can be expressed in terms of single-layer operators. In fact, in view of (10a), it is clear that forming the impedance matrix Z entails evaluation of integrals corresponding to the Galerkin BEM discretization of the Helmholtz single-layer operator.

In what follows, we thus restrict ourselves to describing the regularization of the single-layer potential (13a), and the regularization of double integrals of the form:

$$\langle\psi,\mathsf{S}\varphi\rangle = \int_\Gamma \psi(\boldsymbol{r})\int_\Gamma G(\boldsymbol{r},\boldsymbol{r}')\varphi(\boldsymbol{r}')\,\mathrm{d}s'\,\mathrm{d}s \tag{16}$$

where ψ and φ are scalar densities, which may correspond to either individual components of the RWG basis functions $\mathbf{f}_n$ (in the case of E_1) or their surface divergence $\nabla_s\cdot\mathbf{f}_n$ (in the case of E_2).

The proposed kernel-regularization technique relies on interpolation of the relevant densities by means of linear combinations of planewaves of the form

$$\Phi(\boldsymbol{r}',\boldsymbol{r}_0) = \sum_{\ell=1}^{L} c_\ell(\boldsymbol{r}_0)\,\mathrm{e}^{ik\boldsymbol{d}_\ell\cdot(\boldsymbol{r}_0-\boldsymbol{r}')} \tag{17}$$

where $\boldsymbol{r}'\in\mathbb{R}^3$ and $\boldsymbol{r}_0\in\Gamma$, with $\boldsymbol{d}_\ell\in\mathbb{R}^3$, $|\boldsymbol{d}_\ell|=1$, $1\le\ell\le L$ denoting planewave directions, which may or may not depend on $\boldsymbol{r}_0\in\Gamma$. Since this linear combination satisfies the homogeneous Helmholtz equation

$$\nabla'^2\Phi(\boldsymbol{r}',\boldsymbol{r}_0) + k^2\Phi(\boldsymbol{r}',\boldsymbol{r}_0) = 0 \quad \text{for all } \boldsymbol{r}'\in\mathbb{R}^3$$

it follows from the Kirchhoff integral formula [38] (also known as Green's third identity or extinction theorem) that the single-layer potential (13a) can be expressed as [24]:

$$\begin{aligned}(\mathcal{S}\varphi)(\boldsymbol{r}) = {}& \int_\Gamma G(\boldsymbol{r},\boldsymbol{r}')\big\{\varphi(\boldsymbol{r}')-\Phi_n(\boldsymbol{r}',\boldsymbol{r}_0)\big\}\,\mathrm{d}s' \\ & + \mathbf{1}_\Omega(\boldsymbol{r})\Phi(\boldsymbol{r},\boldsymbol{r}_0) + \int_\Gamma \frac{\partial G(\boldsymbol{r},\boldsymbol{r}')}{\partial\hat{\mathbf{n}}'}\Phi(\boldsymbol{r}',\boldsymbol{r}_0)\,\mathrm{d}s'\end{aligned} \tag{18}$$

for all $\boldsymbol{r}\in\mathbb{R}^3\setminus\Gamma$. Here, $\Phi_n(\boldsymbol{r}',\boldsymbol{r}_0)=\hat{\mathbf{n}}'\cdot\nabla'\Phi(\boldsymbol{r}',\boldsymbol{r}_0)$ and the function $\mathbf{1}_\Omega$ denotes the indicator function of the domain Ω, that is, $\mathbf{1}_\Omega(\boldsymbol{r})=1$ if $\boldsymbol{r}\in\Omega$ and $\mathbf{1}_\Omega(\boldsymbol{r})=0$ if $\boldsymbol{r}\in\mathbb{R}^3\setminus\overline{\Omega}$. Note that the last integral above corresponds to the Helmholtz double-layer potential (13b) applied to the interpolant $\Phi(\cdot,\boldsymbol{r}_0)$.

Therefore, using the jump relations (15), the following equivalent formula for (16) is found:

$$\begin{aligned}\langle\psi,\mathsf{S}\varphi\rangle = {}& \frac{1}{2}\int_\Gamma \psi(\boldsymbol{r})\Phi(\boldsymbol{r},\boldsymbol{r}_0)\,\mathrm{d}s \\ & + \int_\Gamma \psi(\boldsymbol{r})\int_\Gamma G(\boldsymbol{r},\boldsymbol{r}')\big\{\varphi(\boldsymbol{r}')-\Phi_n(\boldsymbol{r}',\boldsymbol{r}_0)\big\}\,\mathrm{d}s'\,\mathrm{d}s \\ & + \int_\Gamma \psi(\boldsymbol{r})\int_\Gamma \frac{\partial G(\boldsymbol{r},\boldsymbol{r}')}{\partial\hat{\mathbf{n}}'}\Phi(\boldsymbol{r}',\boldsymbol{r}_0)\,\mathrm{d}s'\,\mathrm{d}s.\end{aligned} \tag{19}$$

Note that, up to this point, we have treated $\boldsymbol{r}_0\in\Gamma$ as a free parameter that we can choose at our convenience. The key idea underlying the proposed regularization technique is that, in order to achieve bounded or even smoother integrands in (19), it suffices to select $\boldsymbol{r}_0=\boldsymbol{r}$ and require $\Phi_n(\cdot,\boldsymbol{r})$ and $\Phi(\cdot,\boldsymbol{r})$ to approximate φ and the zero density, respectively, at the point $\boldsymbol{r}'=\boldsymbol{r}$ (precisely where the integral kernels become singular). This is achieved here by asking $\Phi(\cdot,\boldsymbol{r})$ to satisfy certain pointwise interpolation conditions. In detail, letting $M_1, M_2\ge0$, these conditions are

$$\lim_{\boldsymbol{r}'\to\boldsymbol{r}}\partial'^{\alpha}_s\Phi(\boldsymbol{r}',\boldsymbol{r}) = 0 \quad \forall|\alpha|\le M_1 \tag{20a}$$

and

$$\lim_{\boldsymbol{r}'\to\boldsymbol{r}} \partial_s'^{\alpha}\{\varphi(\boldsymbol{r}') - \Phi_n(\boldsymbol{r}',\boldsymbol{r})\} = 0 \quad \forall|\alpha| \le M_2 \tag{20b}$$

where $\partial_s'^{\alpha}$, with $\alpha = (\alpha_1, \alpha_2) \in \mathbb{N}^2$ and $|\alpha| = \alpha_1 + \alpha_2$, denotes the $|\alpha|$th order tangential derivative on Γ (with respect to $\boldsymbol{r}'$). It follows from (20) that the integrands in (19) satisfy:

$$\left|G(\boldsymbol{r},\boldsymbol{r}')\{\varphi(\boldsymbol{r}') - \Phi_n(\boldsymbol{r}',\boldsymbol{r})\}\right| \lesssim \left|\boldsymbol{r}-\boldsymbol{r}'\right|^{M_2} \tag{21a}$$

$$\left|\frac{\partial G(\boldsymbol{r},\boldsymbol{r}')}{\partial\hat{\mathbf{n}}'}\Phi(\boldsymbol{r}',\boldsymbol{r})\right| \lesssim \left|\boldsymbol{r}-\boldsymbol{r}'\right|^{M_1} \tag{21b}$$

in a neighborhood of $\boldsymbol{r} \in \Gamma$, provided that Φ fulfills the conditions (20). This means that the integrands in (19) become bounded or even smoother functions of $\boldsymbol{r}' \in \Gamma$ whenever $M_1, M_2 \ge 0$ and, thus, their integral can be approximated by standard quadrature rules.

Note that in the derivations presented earlier, we have assumed that the scalar density φ is sufficiently smooth in a neighborhood B of the interpolation point $\boldsymbol{r} \in \Gamma$. Concurrently, we have assumed that there exists a sufficiently smooth local parameterization $\mathbf{X} : D \subset \mathbb{R}^2 \to B \subset \Gamma$ around $\boldsymbol{r} \in B$ so that the tangential derivatives of a density function $\varphi : \Gamma \to \mathbb{C}$ exist and are given by $\partial_s^{\alpha}\varphi(\boldsymbol{r}) = (\partial^{\alpha_1}/\partial\xi_1^{\alpha_1})(\partial^{\alpha_2}/\partial\xi_2^{\alpha_2})\varphi(\mathbf{X}(\xi_1,\xi_2))$, with $\alpha = (\alpha_1, \alpha_2)$. In general, none of these assumptions hold globally. The scalar components of the RWG basis functions, for example, are not even continuous on the whole surface Γ. Therefore, special care has to be taken in selecting quadrature points for the evaluation of the outer integrals in (19), to make sure that these assumptions are actually satisfied at those points $\boldsymbol{r} \in \Gamma$ (see Section VI-A for details).

Similarly, the regularization of the nearly singular kernels in the on-surface integral operators $\mathcal{E}$ in (3)—at points $\boldsymbol{r} \in \mathbb{R}^3 \setminus \Gamma$ close to but not on Γ—uses the fact that $\mathcal{E}_1$ (resp. $\mathcal{E}_2$) can be expressed in terms of the Helmholtz single-layer potential (resp. gradient of the single-layer potential) applied to a vector (resp. scalar) density function. Regularization of the kernels, in this case, can be effected by selecting $\boldsymbol{r}_0 \in \Gamma$ in (18) as the projection of the target point $\boldsymbol{r} \in \mathbb{R}^3 \setminus \Gamma$ on the surface, i.e., $\boldsymbol{r}_0 = \operatorname{argmin}_{r'\in\Gamma}|\boldsymbol{r}-\boldsymbol{r}'|$ [24], [25]. Doing so, the integrands in the single-layer potentials present in $\mathcal{E}_1$ satisfy

$$\left|G(\boldsymbol{r},\boldsymbol{r}')\{\varphi(\boldsymbol{r}') - \Phi_n(\boldsymbol{r}',\boldsymbol{r}_0)\}\right| \lesssim \left|\boldsymbol{r}_0-\boldsymbol{r}'\right|^{M_2} \tag{22a}$$

$$\left|\frac{\partial G(\boldsymbol{r},\boldsymbol{r}')}{\partial\hat{\mathbf{n}}'}\Phi(\boldsymbol{r}',\boldsymbol{r}_0)\right| \lesssim \left|\boldsymbol{r}_0-\boldsymbol{r}'\right|^{M_1-1} \tag{22b}$$

while the kernels in the gradient of the single-layer potential present in $\mathcal{E}_2$ satisfy

$$\left|\nabla G(\boldsymbol{r},\boldsymbol{r}')\{\varphi(\boldsymbol{r}') - \Phi_n(\boldsymbol{r}',\boldsymbol{r}_0)\}\right| \lesssim \left|\boldsymbol{r}_0-\boldsymbol{r}'\right|^{M_2-1} \tag{23a}$$

$$\left|\nabla\frac{\partial G(\boldsymbol{r},\boldsymbol{r}')}{\partial\hat{\mathbf{n}}'}\Phi(\boldsymbol{r}',\boldsymbol{r}_0)\right| \lesssim \left|\boldsymbol{r}_0-\boldsymbol{r}'\right|^{M_1-2}. \tag{23b}$$

Exactly, the same strategy can be applied to the regularization of the kernels in integrals of the form (12) arising in the multiple-scattering EFIE formulation. The optimal point $\boldsymbol{r}_0$ in the corresponding regularized form of the single-layer potential is $\boldsymbol{r}_0 = \operatorname{argmin}_{\boldsymbol{r}'\in\Gamma_j}|\boldsymbol{r}-\boldsymbol{r}'|$ where $\boldsymbol{r} \in \Gamma_i$ in this case. The actual practical procedure used to select the regularization point $\boldsymbol{r}_0$ used in the MoM discretization of the EFIE is discussed in Section VI-A.

Sections V-A and V-B present the procedures to construct planewave density interpolants (17): a low-order ($M_1 = M_2 = 1$) analytical procedure and a higher order least-squares procedure.

A. Closed-Form PWDI

In order to construct the planewave density interpolant (17), we rewrite it as

$$\Phi(\boldsymbol{r}',\boldsymbol{r}) := \sum_{|\alpha|=0,1} \partial_s^{\alpha}\varphi(\boldsymbol{r})\Phi_{\alpha}(\boldsymbol{r}',\boldsymbol{r}) \tag{24}$$

where each function Φ_α for $|\alpha| \le 1$ is a linear combinations of planewaves. Therefore, according to the interpolation conditions (20) for $M_1 = M_2 = 1$, the expansion functions in (24) must fulfill

$$\partial_s^{\beta}\Phi_{\alpha}(\boldsymbol{r},\boldsymbol{r}) = 0 \quad \text{and} \quad \partial_s^{\beta}\Phi_{n,\alpha}(\boldsymbol{r},\boldsymbol{r}) = \begin{cases} 1, & \text{if } \beta = \alpha \\ 0, & \text{if } \beta \ne \alpha \end{cases} \tag{25}$$

at $\boldsymbol{r}' = \boldsymbol{r}$ for $|\beta| \le 1$. As it turns out [24], explicit analytical expressions for these functions can be derived. Indeed, letting $\hat{\boldsymbol{\tau}}_j$, $j = 1, 2$, denote linearly independent unit surface tangent vectors at $\boldsymbol{r} \in \Gamma$, and further assuming that $\hat{\boldsymbol{\tau}}_1 \cdot \hat{\boldsymbol{\tau}}_2 = 0$ and $\hat{\boldsymbol{\tau}}_1 \times \hat{\boldsymbol{\tau}}_2 = \hat{\mathbf{n}}$, we have that

$$\Phi_{(0,0)}(\boldsymbol{r}',\boldsymbol{r}) := \frac{1}{k}\sin\big(k\hat{\mathbf{n}}\cdot(\boldsymbol{r}'-\boldsymbol{r})\big) \tag{26a}$$

$$\Phi_{(1,0)}(\boldsymbol{r}',\boldsymbol{r}) := \frac{2}{k^2}\sin\left(\frac{k\hat{\mathbf{n}}}{\sqrt{2}}\cdot(\boldsymbol{r}'-\boldsymbol{r})\right)\sin\left(\frac{k\hat{\boldsymbol{\tau}}_1}{\sqrt{2}}\cdot(\boldsymbol{r}'-\boldsymbol{r})\right) \tag{26b}$$

$$\Phi_{(0,1)}(\boldsymbol{r}',\boldsymbol{r}) := \frac{2}{k^2}\sin\left(\frac{k\hat{\mathbf{n}}}{\sqrt{2}}\cdot(\boldsymbol{r}'-\boldsymbol{r})\right)\sin\left(\frac{k\hat{\boldsymbol{\tau}}_2}{\sqrt{2}}\cdot(\boldsymbol{r}'-\boldsymbol{r})\right) \tag{26c}$$

satisfy (25) and, therefore, (24) satisfies the point conditions (20) for the interpolation orders, we were looking for [24].

B. Numerical PWDI

An algebraic approach to find the coefficients $\{c_\ell(\boldsymbol{r})\}_{\ell=1}^{\ell=L}$ in the PWDI expansion (17) at a given point $\boldsymbol{r} \in \Gamma$ is presented in this section. Unlike the analytical approach, a collection of planewave directions $\{\boldsymbol{d}_\ell\}_{\ell=1}^{\ell=L}$ that are independent of the point $\boldsymbol{r} \in \Gamma$ is used. While the desired interpolation orders M_j, $j = 1, 2$, and the number L of planewave directions are parameters in the algorithm, the planewave directions themselves can be selected either randomly or uniformly from the unit sphere in three dimensions (an appropriate selection of planewave directions is provided in Section VI-B).

In order to find the desired expansion coefficients, one has to impose a number $D_1 = (M_1+1)(M_1+2)/2$ of independent conditions (20a) as well as $D_2 = (M_2+1)(M_2+2)/2$ independent conditions (20b), which have to be satisfied exactly. Consequently, a solvable linear system for the coefficients could be produced, provided that the number of planewave directions

satisfies $L \geq D_1 + D_2$. In order to form such a linear system, we proceed to sort the indices $\alpha = (\alpha_1, \alpha_2)$ satisfying $|\alpha| = \alpha_1 + \alpha_2 \leq \max\{M_1, M_2\}$ by introducing a bijective mapping $f : \{|\alpha| \leq \max\{M_1, M_2\}\} \to \{1, \ldots, \max\{D_1, D_2\}\}$. Therefore, letting $\mathbf{b}(\boldsymbol{r}) \in \mathbb{C}^D$, where $(\mathbf{b}(\boldsymbol{r}))_n = 0$, $1 \leq n \leq D_1$ and $(\mathbf{b}(\boldsymbol{r}))_n = \partial_s^{f^{-1}(n)}\varphi(\boldsymbol{r})$, $1 \leq n \leq D_2$, we have that conditions (20) lead to the linear system

$$A(\boldsymbol{r})\mathbf{c}(\boldsymbol{r}) = \mathbf{b}(\boldsymbol{r}) \tag{27}$$

for the coefficient vector $\mathbf{c}(\boldsymbol{r}) = [c_1(\boldsymbol{r}), \ldots, c_L(\boldsymbol{r})]^T \in \mathbb{C}^L$, where $A(\boldsymbol{r})$ is a $(D_1 + D_2) \times L$ complex-valued matrix that depends on the planewave directions and the local geometry of the surface Γ at the point $\boldsymbol{r}$. Note that we have assumed in these derivations that the first D_1 rows of $A(\boldsymbol{r})$ correspond to the conditions (20a) on $\Phi(\cdot, \boldsymbol{r})$, whereas the remaining D_2 rows correspond to the conditions (20b) on $\Phi_n(\cdot, \boldsymbol{r})$ sorted according to the bijective mapping f.

As it turns out the matrix, $A(\boldsymbol{r})$ can be easily constructed at points where the surface is locally flat [24]. In fact, for interpolation orders $M_1 = M_2 = 3$, the column of the $A(\boldsymbol{r})$ associated with the planewave direction $\boldsymbol{d}_\ell$ is given by $[\mathbf{a}_\ell(\boldsymbol{r}), \tau_2\mathbf{a}_\ell(\boldsymbol{r})]^T$, where $\mathbf{a}_\ell = [1, \tau_1, \tau_2, \tau_1^2, \tau_1\tau_2, \tau_2^2, \tau_1^3, \tau_1^2\tau_2, \tau_1\tau_2^2, \tau_2^3]$ with $\tau_1 = ik\boldsymbol{d}_\ell \cdot \hat{\boldsymbol{\tau}}_1$, $\tau_2 = ik\boldsymbol{d}_\ell \cdot \hat{\boldsymbol{\tau}}_2$ and $\tau_3 = ik\boldsymbol{d}_\ell \cdot \hat{\mathbf{n}}$, and the bijective mapping defined by $f(0,0) = 1$, $f(1,0) = 2$ $f(0,1) = 3$, $f(2,0) = 4$, $f(1,1) = 5$, $f(0,2) = 6$, $f(3,0) = 7$, $f(2,1) = 8$, $f(1,2) = 9$, and $f(0,3) = 10$.

VI. Implementation Details

A. Quadrature Rule

This section describes a straightforward quadrature rule for numerical integration over triangulated surfaces that will be used in the approximation of the regularized surface integrals produced by the PWDI method.

First, we focus on the double integral (16), which upon discretization of the surface Γ into planar triangles becomes

$$\langle \psi, \mathsf{S}\varphi \rangle = \sum_{i=1}^{N_h} \int_{T_i} \psi(\boldsymbol{r})(\mathsf{S}\varphi)(\boldsymbol{r})\, \mathrm{d}s \tag{28}$$

with

$$(\mathsf{S}\varphi)(\boldsymbol{r}) = \sum_{j=1}^{N_h} \int_{T_j} K(\boldsymbol{r}, \boldsymbol{r}')\, \mathrm{d}s' \tag{29}$$

where the regularized integrand above is given by

$$K(\boldsymbol{r}, \boldsymbol{r}') = G(\boldsymbol{r}, \boldsymbol{r}')\{\varphi(\boldsymbol{r}') - \Phi_n(\boldsymbol{r}', \boldsymbol{r})\} + \frac{\partial G(\boldsymbol{r}, \boldsymbol{r}')}{\partial \hat{\mathbf{n}}'}\Phi(\boldsymbol{r}', \boldsymbol{r}).$$

Note that the term involving $\Phi(\boldsymbol{r}, \boldsymbol{r})$ has been omitted here as it has been already assumed that $\Phi(\cdot, \boldsymbol{r})$ interpolates the zero density at $\boldsymbol{r} \in \Gamma$.

We recall now that the construction of Φ requires both the scalar density φ and the surface Γ to be smooth in a neighborhood of $\boldsymbol{r} \in \Gamma$. In order to fulfill these conditions, we utilize the (interior) quadrature points [39]

$$\tilde{\boldsymbol{v}}_m^{(i)} := \sum_{\ell=1}^{3} \frac{(1 + 3\delta_{m,\ell})}{6} \boldsymbol{v}_\ell^{(i)}, \quad 1 \leq m \leq 3,\ 1 \leq i \leq N_h \tag{30}$$

to evaluate the integrals on the triangles T_i, where $\boldsymbol{v}_\ell^{(i)}$, $1 \leq \ell \leq 3$, denote the vertices of T_i. Application of this quadrature rule yields the following approximation:

$$\langle \psi, \mathsf{S}\varphi \rangle \approx \sum_{i=1}^{N_h} \frac{A_i}{3} \sum_{m=1}^{3} \psi(\tilde{\boldsymbol{v}}_m^{(i)})(\mathsf{S}\varphi)(\tilde{\boldsymbol{v}}_m^{(i)}) \tag{31}$$

of (28), where A_i is the area of T_i. Given that the quadrature points $\tilde{\boldsymbol{v}}_m^{(i)}$ lie in the interior of T_i, we use for the computation of the planewave interpolant Φ the unit normal $\hat{\mathbf{n}}$ to T_i and orthogonal unit vectors $\hat{\boldsymbol{\tau}}_\ell$, $\ell = 1, 2$, tangential to T_i.

The values of the single-layer operator at the quadrature points $\tilde{\boldsymbol{v}}_m^{(i)}$, $1 \leq m \leq 3$, which are needed in (31), are approximated as

$$(\mathsf{S}\varphi)(\boldsymbol{r}) = \sum_{i=1}^{N_h} \int_{T_i} K(\boldsymbol{r}, \boldsymbol{r}')\, \mathrm{d}s' \approx \sum_{i=1}^{N_h} \frac{A_i}{3} \sum_{m=1}^{3} K(\boldsymbol{r}, \tilde{\boldsymbol{v}}_m^{(i)}) \tag{32}$$

for $\boldsymbol{r} \in \Gamma$, using the same interior-point quadrature rule, but any other sufficiently accurate quadrature over triangles can be used.

Similarly, the regularized single-layer potential (18) is approximated as

$$(\mathcal{S}\varphi)(\boldsymbol{r}) = \sum_{i=1}^{N_h} \int_{T_i} K_0(\boldsymbol{r}, \boldsymbol{r}')\, \mathrm{d}s' \approx \sum_{i=1}^{N_h} \frac{A_i}{3} \sum_{m=1}^{3} K_0(\boldsymbol{r}, \tilde{\boldsymbol{v}}_m^{(i)}) \tag{33}$$

for $\boldsymbol{r} \in \mathbb{R}^3 \setminus \overline{\Omega}$, where the regularized integrand in this case takes the form

$$K_0(\boldsymbol{r}, \boldsymbol{r}') = G(\boldsymbol{r}, \boldsymbol{r}')\{\varphi(\boldsymbol{r}') - \Phi_n(\boldsymbol{r}', \boldsymbol{r}_0)\} + \frac{\partial G(\boldsymbol{r}, \boldsymbol{r}')}{\partial \hat{\mathbf{n}}'}\Phi(\boldsymbol{r}', \boldsymbol{r}_0) \tag{34}$$

with the interpolation point $\boldsymbol{r}_0 \in \Gamma$ selected as explained in what follows. For any given target point $\boldsymbol{r}$, we first find the surface triangle T_{i^*} whose center is the closest to the point $\boldsymbol{r}$. The interpolation point is then selected as $\boldsymbol{r}_0 = \tilde{\boldsymbol{v}}_{m^*}^{(i^*)}$, where $\tilde{\boldsymbol{v}}_{m^*}^{(i^*)}$ is the (interior) quadrature point in T_{i^*} that is the closest to $\boldsymbol{r}$. Accordingly, the construction of the planewave interpolant uses the unit normal and tangent vectors to T_{i^*}. Note that this choice of $\boldsymbol{r}_0$ ensures that the limit (15a) holds for the discretized single-layer operator (32) and potential (33). The gradient of the regularized single-layer potential—which is also needed for the computation of the off-surface operator $\mathcal{E}$—is approximated following the same procedure applied to ∇K_0 instead of K_0.

Finally, we consider the case in which $\Gamma = \Gamma_1 \cup \Gamma_2$ is a composite surface in the sense defined in Section IV. The scalar density φ in this case has two components: φ_1 and φ_2 defined on Γ_1 and Γ_2, respectively. Letting that $\mathcal{S}_j$ denotes the regularized single-layer potentials defined by integration on the closed surface Γ_j, $j = 1, 2$, we have that the whole potential naturally splits as $\mathcal{S}\varphi = \mathcal{S}_1\varphi_1 + \mathcal{S}_2\varphi_2$ into two terms, each of which can be discretized and evaluated everywhere—in $\mathbb{R}^3 \setminus \overline{\Omega}$ and Γ—following the procedure described earlier using separate meshes for Γ_1 and Γ_2. These potentials are also utilized to compute the double integrals for the construction of the Galerkin impedance matrix. In fact, letting that ψ_1 and ψ_2

denote the components of ψ defined on Γ_1 and Γ_2, we have

$$\langle \psi, \mathsf{S}\varphi \rangle = \langle \psi_1, (\mathcal{S}_2\varphi_2)|_{\Gamma_1} \rangle + \langle \psi_2, (\mathcal{S}_1\varphi_1)|_{\Gamma_2} \rangle + \langle \psi_1, (\mathcal{S}_1\varphi_1)|_{\Gamma_1} \rangle + \langle \psi_2, (\mathcal{S}_2\varphi_2)|_{\Gamma_2} \rangle \quad (35)$$

where each of the integrals $\langle \psi_i, (\mathcal{S}_j\varphi_j)|_{\Gamma_i} \rangle$ over Γ_i $(i, j = 1, 2)$ can be approximated using the interior-point quadrature rule described earlier.

B. Selection of Planewave Directions

As was discussed in Section V-B, the high-order algebraic approach for the construction of the planewave interpolant requires the explicit selection of $L \geq D_1 + D_2$ planewave directions where $D_1 = (M_1 + 1)(M_1 + 2)/2$ and $D_2 = (M_2+1)(M_2+2)/2$ depend on the interpolation orders $M_1 \geq 0$ and $M_2 \geq 0$. We have observed in numerical experiments that the minimal choice $L = D_1 + D_2$ results in a square matrix $A(\boldsymbol{r})$ that is very ill conditioned for some points $\boldsymbol{r} \in \Gamma$. Therefore, we recommend in general to select $L > D_1 + D_2$ in order to sufficiently enrich the column space of $A(\boldsymbol{r})$ so that its pseudoinverse, denoted by $A^{\dagger}(\boldsymbol{r})$, becomes computable. In practice, large enough $\mathcal{O}(M_1 M_2)$ numbers of planewave directions selected from a "uniform" spherical grid give rise to numerically invertible matrices $A(\boldsymbol{r})A^*(\boldsymbol{r})$ from where $A^{\dagger}(\boldsymbol{r})$ can be computed. In detail, the planewave directions for the construction of numerical PWDI interpolants used throughout this article are given by $(\cos\theta_m \sin\phi_n, \sin\theta_m \sin\phi_n, \cos\phi_n)$, where $\theta_m = 2\pi(m - 1/2)/L_\theta$ for $m = 1, \ldots, L_\theta$ and $\phi_n = \pi(n - 1/2)/L_\phi$ for $n = 1, \ldots, L_\phi$, with $L = L_\theta \times L_\phi = 2 \times 2, 4 \times 3, 5 \times 4, 6 \times 5$ for interpolation orders $\max\{M_1, M_2\} = 0, 1, 2, 3$, respectively.

C. Tangential Derivatives of RWG Basis Functions

The RWG basis functions associated with the mesh edges are defined as [1]

$$\mathbf{f}_n(\boldsymbol{r}) := \begin{cases} \pm\dfrac{L_n}{2A_n^{\pm}}\big(\boldsymbol{v}^{\pm} - \boldsymbol{r}\big), & \boldsymbol{r} \in T_n^{\pm} \\ \mathbf{0}, & \boldsymbol{r} \notin T_n^{\pm} \end{cases} \quad (36)$$

where T_n^+ and T_n^- denote the triangles of areas A_n^+ and A_n^-, respectively, that share the nth edge of length L_n.

The tangential derivatives of the RWG functions can be easily computed by differentiating (36) and taking the dot product with the tangential unit vectors $\hat{\boldsymbol{\tau}}_\ell^{\pm}$, $\ell = 1, 2$, associated with the corresponding triangles $T_n^{\pm}$. We thus have

$$\big(\partial_s^{\alpha}\mathbf{f}_n\big)(\boldsymbol{r}) = \begin{cases} \mp\dfrac{L_n}{2A_n^{\pm}}\hat{\boldsymbol{\tau}}_1^{\pm}(\boldsymbol{r}), & \boldsymbol{r} \in T_n^{\pm},\ \alpha = (1, 0) \\ \mp\dfrac{L_n}{2A_n^{\pm}}\hat{\boldsymbol{\tau}}_2^{\pm}(\boldsymbol{r}), & \boldsymbol{r} \in T_n^{\pm},\ \alpha = (0, 1) \\ \mathbf{0}, & \boldsymbol{r} \notin T_n^{\pm} \text{ or } |\alpha| > 1 \end{cases} \quad (37)$$

and it also follows from (37) that the tangential derivative of the surface divergence is given by:

$$\partial_s^{\alpha}(\nabla_s \cdot \mathbf{f}_n)(\boldsymbol{r}) = \begin{cases} \mp\dfrac{L_n}{A_n^{\pm}}, & \boldsymbol{r} \in T_n^{\pm},\ \alpha = (0, 0) \\ 0, & \boldsymbol{r} \notin T_n^{\pm} \text{ or } |\alpha| > 0. \end{cases}$$

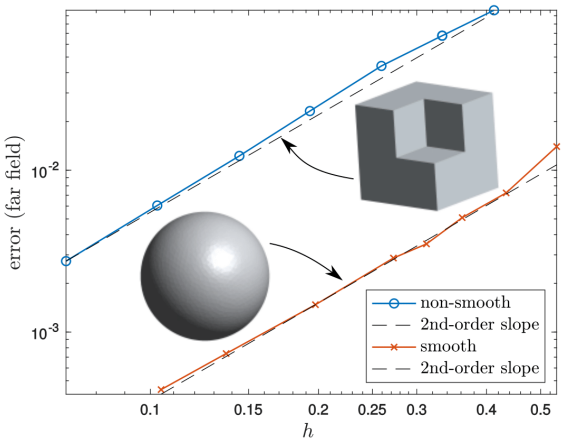

Fig. 1. Convergence of the far-field errors in the scattered field computed by means of the MoM using the analytical PWDI kernel-regularization procedure of Section V-A and the interior-point quadrature rule of Section VI-A.

VII. Validation and Examples

This section presents a variety of numerical examples to validate and demonstrate the capabilities of the PWDI method.

In what follows, we let $\mathbf{E}^{\mathrm{s}}$ denote the MoM-computed scattered electric field and $\mathbf{E}^{\mathrm{ref}}$ denote an either exact or highly accurate reference solution. The far- and near-field errors shown in some of the validation examples below are then computed by means of the formula

$$\text{error} = \max_{\boldsymbol{r}\in S}\big|\mathbf{E}^{s}(\boldsymbol{r}) - \mathbf{E}^{\mathrm{ref}}(\boldsymbol{r})\big| \,/\, \max_{\boldsymbol{r}\in S}\big|\mathbf{E}^{\mathrm{ref}}(\boldsymbol{r})\big| \quad (38)$$

with S denoting a set of sample target points. The set S used in (38) depends on the kind of error—in the far or near field—that is to be measured. The far-field errors presented in the error plots in Sections VII-A and VII-B, in particular, are computed by taking S as the set of mesh nodes corresponding to a large sphere of radius $r = 100$ m centered at the origin, which encloses the surface Γ under consideration.

A. Single Surfaces

The examples of this section have been designed to validate the proposed methodology when applied to the solution of standard problems of scattering by single PEC obstacles bounded by closed and simply connected surfaces. The frequency $f \approx 75$ MHz (corresponding to the wavenumber $k = 0.5\pi$ rad/m and the wavelength $\lambda = 4$ m) is used in the examples of this section. We consider both a smooth surface and a more general Lipschitz surface featuring a reentrant corner at the origin. Specifically, these surfaces are, respectively, a sphere of radius 1 m centered at the origin and the boundary of the domain corresponding to a cube centered at the origin of side length 1 m without the subdomain contained in the first (+++) octant (see the inset in Fig. 1). The analytical PWDI approach of Section V-A is utilized here, but almost identical results are also obtained using the higher order algebraic procedure presented in Section V-B. This might be because the Galerkin approximation errors dominate over the errors introduced by the numerical evaluation of the

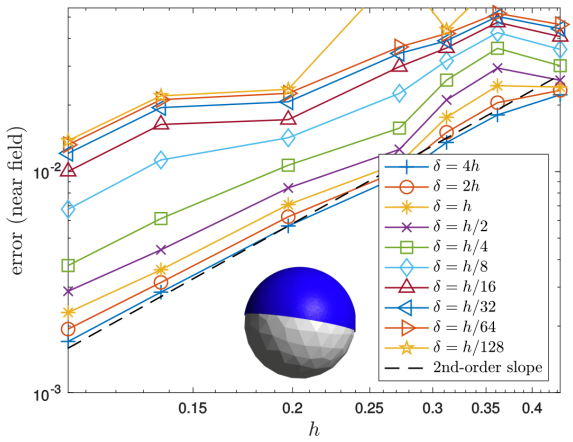

(a)

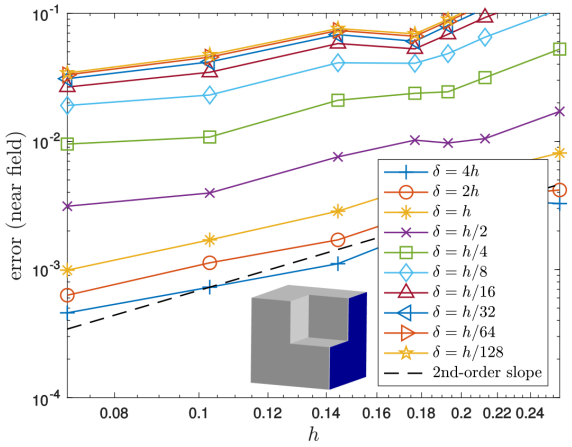

(b)

Fig. 2. Convergence of the near-fields errors in the solution of a scattering problem from (a) smooth and (b) nonsmooth closed surface. The near-fields errors are empirically estimated using (38) evaluating the fields at open surfaces S that are parallel to the closed surfaces Γ under consideration. The evaluation surfaces S, which are placed at a distance δ from the closed surfaces, are depicted in blue in the inset figures.

PWDI kernel-regularized integrals. Fig. 1 shows the far-field errors obtained for various mesh sizes h (in meters). Clearly, the expected second-order convergence of the far-field errors (i.e., error $\propto h^2$) is observed in both cases. These errors were measured by means of (38) with an exact closed-form solution used as the reference $\mathbf{E}^{\text{ref}}$. Such an exact solution is manufactured by setting the dipole $\mathbf{E}^{\text{inc}}(\boldsymbol{r}) = -\nabla \times \{G(\boldsymbol{r}, \boldsymbol{r}')\boldsymbol{p}\}$, located at a point $\boldsymbol{r}' \in \Omega$ inside the closed surface, as the incident electric field. Indeed, it can be shown that the (unique) scattered electric field solution of the scattering problem is given by $\mathbf{E}^s(\boldsymbol{r}) = \nabla \times \{G(\boldsymbol{r}, \boldsymbol{r}')\boldsymbol{p}\}$ ($\boldsymbol{r} \in \mathbb{R}^3 \setminus \Omega$) in this case. The polarization vector $\boldsymbol{p} = (1, 1, 1)$ and the dipole location $\boldsymbol{r}' = (-0.1, -0.1, -0.25)$ were used in both smooth and nonsmooth cases considered.

Fig. 2, on the other hand, shows the near-field errors corresponding to the same example problems, which were produced by means of (38) with sample target points S on evaluation surfaces that are "parallel" to Γ and placed at a distance $\delta > 0$ from Γ. These evaluation surfaces are shown in blue in the inset of Fig. 2. The higher order interpolation

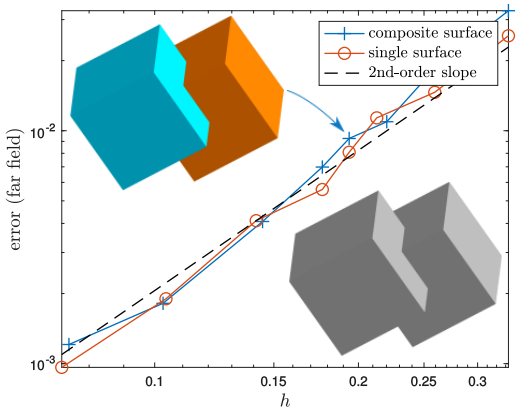

Fig. 3. Far-field errors in the scattered fields produced by the proposed methodology applied to both the classical single-surface and the novel multiple-scattering EFIE formulations for various mesh sizes h.

procedure of Section V-B, with interpolation orders $M_1 = M_2 = 3$, is used here. Note that according to the estimates (22) and (23) interpolation orders $M_1, M_2 > 1$ are needed in order to effectively regularize the off-surface EFIE operator $\mathcal{E}$ from where the scattered electric field is retrieved. As is well known, the accuracy of the MoM-produced off-surface EFIE operator depends not only on the distance of the target point to the surface but also on the local mesh size h near the target point. Therefore, in order to account for the joint effect on the near-field error of these two variables, we set the evaluation surfaces at various distances δ from Γ with δ being selected proportional to the mesh size h. As the results show, nearly second-order convergence of the near-field errors is achieved in all the cases considered. Significant accuracy deterioration is observed, however, for any fixed h as δ becomes smaller. This deterioration is more substantial in the case of the nonsmooth surface. This is explained by the fact that the limited smoothness of the EFIE solution $\mathbf{J}$ at and around corners and edges has a direct impact on the effectiveness of the interpolation procedure.

B. Composite Surfaces

In our next example, we consider a composite surface Γ formed by two overlapping surfaces $\Gamma_1 = \partial\Omega_1$ and $\Gamma_2 = \partial\Omega_2$. Specifically, these are the nonsmooth surface Γ_1 of the previous example—which is rendered in turquoise in the inset of Fig. 3—and the boundary Γ_2 of a cube Ω_2 of side length one contained in first octant—which is rendered in orange in the inset of Fig. 3. We use here the incident field $\mathbf{E}^{\text{inc}}$ given by the superposition of two dipoles placed at $\boldsymbol{r}_1' = (-0.1, 0.1, -0.25) \in \Omega_1$ and $\boldsymbol{r}_2' = (0.6, 0.6, 0.75) \in \Omega_2$ with polarizations $\boldsymbol{p}_2 = (1, 1, 1)$ and $\boldsymbol{p}_2 = (1, -1, 1)$, respectively. As in the previous example, the associated scattering problem has an exact closed-form solution given by $\mathbf{E}^s(\boldsymbol{r}) = \nabla \times \{G(\boldsymbol{r}, \boldsymbol{r}_1')\boldsymbol{p}_1 + G(\boldsymbol{r}, \boldsymbol{r}_2')\boldsymbol{p}_2\}$ that was used in (38) as the reference field to produce the error curves in Fig. 3. Both single- (standard) and multiple-scattering EFIE formulations—posed on $\partial(\overline{\Omega_1} \cup \overline{\Omega_2})$ and on $\Gamma = \Gamma_1 \cup \Omega_2$, respectively—are discretized and solved by means of the PWDI kernel-regularized MoM, which makes use of just one surface mesh of $\partial(\overline{\Omega_1} \cup \overline{\Omega_2})$ in the single-surface formulation,

and nonconformal overlapping surface meshes for Γ_1 and Γ_2 in the multiple-scattering formulation. The convergence results at $f \approx 75$ MHz ($k = 0.5\pi$ rad/m) are presented in Fig. 3, which displays the far-field errors produced by the two approaches for various mesh sizes h. The analytical PWDI procedure of Section V-A was used in this example (the higher order procedure of Section V-B produces almost identical results). Nearly, uniform meshes of all the surfaces involved where used in this example (no mesh refinement was performed around edges or corners). As can be observed in this figure, the second-order convergence of the far-field errors is obtained as $h \to 0$ for both single- and multiple-scattering EFIE formulations and, furthermore, excellent agreement of the two is observed.

Keeping the PEC structure of the previous example, we consider now the problem of scattering of the planewave $\mathbf{E}^{\text{inc}}(\boldsymbol{r}) = (\boldsymbol{p} \times \boldsymbol{d})\, \mathrm{e}^{ik\boldsymbol{d}\cdot\boldsymbol{r}}$ with $\boldsymbol{p} = (0, 0, 1)$, $\boldsymbol{d} = (0, 1, 0)$ and $f \approx 0.3$ GHz ($k = 2\pi$ rad/m, $\lambda = 1$ m). Once again, for validation purposes, the two single- and multiple-scattering EFIE formulations are used, in which nearly uniform meshes of size $h \approx 0.1$ m $= \lambda/10$ are utilized. The resulting surface currents are shown in magnitude format in Fig. 4(a) and (b) corresponding to the EFIE solutions obtained using single conforming and composite nonconforming surface meshes, respectively. Note that the large current densities around the edges of the structure are well captured by the two solution approaches. The associated radar cross sections (RCSs) are shown in Fig. 4(c) at zero elevation angle, where they are also compared against a reference RCS obtained using a significantly refined single conforming surface mesh ($h = 0.075$ m). As can be seen in that figure, the three RCSs are almost indistinguishable.

Next, we consider an even more challenging PEC structure involving three touching spheres: Γ_1, Γ_2, and Γ_3 of radii $r_1 = 0.5$ m, $r_2 = 0.4$ m, and $r_3 = 0.6$ m that are centered at $\boldsymbol{c}_1 = (-0.5, 0, 0)$, $\boldsymbol{c}_2 = (0.4, 0, 0)$, and $\boldsymbol{c}_3 \approx (0.0667, 0.9428, 0.0)$, respectively. We first estimate the numerical errors using (38) by manufacturing an exact solution of the scattering problem. This is done in this case by placing dipoles inside each one of the corresponding spheres, at $\boldsymbol{r}'_1 = (-0.45, 0.05, 0.125)$, $\boldsymbol{r}'_2 = 0.36, -0.04, -0.1)$, and $\boldsymbol{r}'_3 = (0.1267, 1.0028, 0.06)$, with associated polarizations $\boldsymbol{p}_1 = (1, -1, 1)$, $\boldsymbol{p}_2 = (1, 1, 1)$, and $\boldsymbol{p}_3 = -\boldsymbol{p}_2$. As expected, the empirically estimated far-field errors, which are presented in Table I, exhibit second-order convergence as $h \to 0$. The three meshes used in each one of the examples reported in the table are approximately of the same size h. No mesh refinement of any kind was used.

Once we have validated the effectiveness of the PWDI procedure for this challenging PEC structure, we move on to consider a more realistic scattering problem in which a planewave $\mathbf{E}^{\text{inc}}(\boldsymbol{r}) = (\boldsymbol{p} \times \boldsymbol{d})\, \mathrm{e}^{ik\boldsymbol{d}\cdot\boldsymbol{r}}$, with $\boldsymbol{p} = (1, 1, 1)$, $\boldsymbol{d} = (0, 1, 0)$, and $f \approx 0.3$ GHz ($k = 2\pi$ rad/m and $\lambda = 1$ m), illuminates the PEC structure. The results for this case are presented in Fig. 5. Surface meshes of approximately the same size $h \approx 0.1$ m $= \lambda/10$ are used in this example. Fig. 5(a) shows the real part of the three Cartesian components of the total electric field $\mathbf{E} = \mathbf{E}^{\text{inc}} + \mathbf{E}^{s}$ on the plane containing the centers of the three spheres, which were produced by

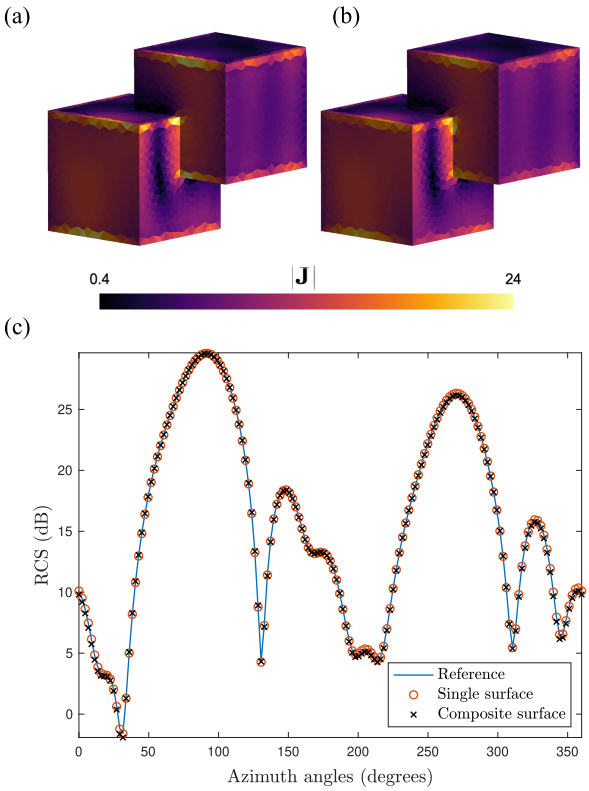

Fig. 4. Comparison of the single-surface and the multiple-scattering EFIE formulations for the solution of a problem of scattering. (a) Magnitude of the surface currents corresponding to the single-surface formulation. (b) Magnitude of the surface currents corresponding to the multiple-scattering formulation. (c) Bistatic RCSs at zero elevation angle.

TABLE I
FAR-FIELD ERRORS RESULTING FROM A CONVERGENCE TEST FOR THE PEC STRUCTURE SHOWN IN FIG. 5 COMPOSED OF THREE TOUCHING SPHERES

h ($\times 10$)	0.69	1.01	1.37	1.64	1.87	2.17	2.67	4.26
error (%)	0.70	1.36	2.35	2.94	3.99	5.78	6.99	24.8

direct evaluation of the off-surface operator $\mathcal{E}$ after being regularized by the algebraic PWDI procedure of Section V-B with $M_1 = M_2 = 3$. As expected, a weak shadow appears in the wake of the PEC structure. Fig. 5(b), on the other hand, shows the surface currents (in magnitude format) at and around the touching points on each one of the three spheres. Finally, Fig. 5(c) shows the associated RCSs together with a reference RCS, which was produced using finer meshes of size $h = 0.075$ m of the three spheres Γ_1, Γ_2, and Γ_3.

C. Comparison of the PWDI With Existing Methods

In order to further validate the proposed PWDI kernel-regularization procedure, we present here a comparison of the analytical PWDI method with both the classical Mie series solution [42, Sec. 11.8] and the popular Duffy-type regularization technique put forth by Sauter and Schwab (SS) [41, Sec. 5]. In detail, we consider the problem of scattering of a planewave off of a PEC sphere of radius $a = \lambda/2 = 1$ m. The problem is solved by means of the analytical PWDI method and a straightforward in-house implementation of the SS regularization where a total of 16 and 81 Gauss quadrature points are used

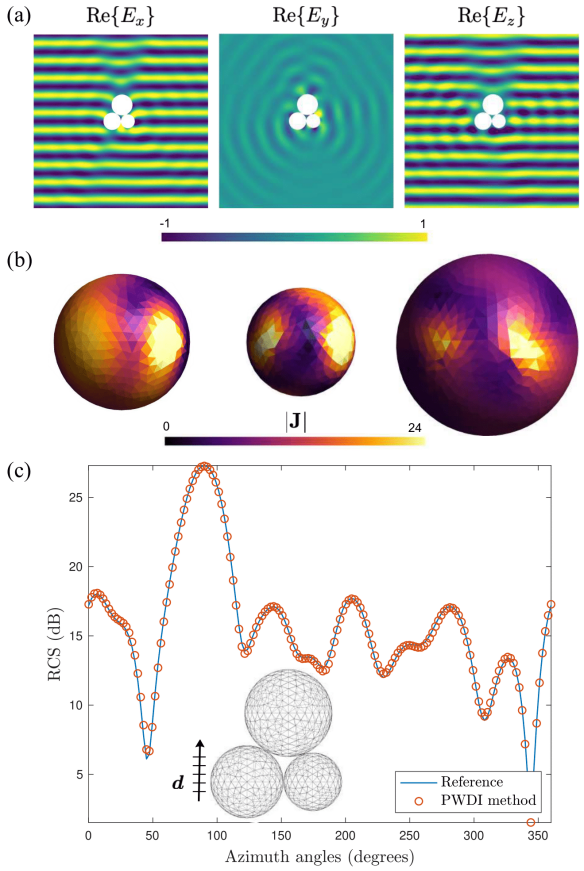

Fig. 5. Electric field and surface currents corresponding to the scattering of a planewave from a PEC structure comprising three touching spheres, computed using the PWDI methodology. (a) Plot of the three components of the total electric field on the xy plane. (b) Magnitude of the currents on each of the spheres. (c) Bistatic RCSs at zero elevation angle.

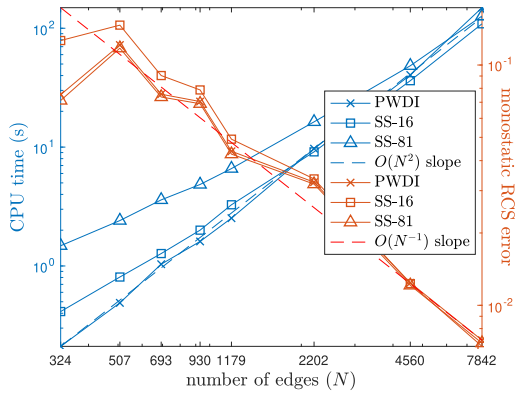

Fig. 6. Blue: time required to form the EFIE matrix using the analytical PWDI approach and using the SS [41] approach in conjunction with a 16-point (SS-16) and an 81-point (SS-81) Gauss quadrature rule. Red: errors in the monostatic RCS resulting from the three methods, which are measured with respect to the value obtained from the Mie series solution.

TABLE II

INTEGRATION ERRORS IN THE DIAGONAL ENTRIES OF THE PWDI-COMPUTED EFIE MATRIX (e) AND CORRESPONDING ERRORS IN THE SYSTEM SOLUTION ($\overline{e}$). ERRORS (MEASURED WITH RESPECT TO THE MIE SOLUTION) IN THE MONOSTATIC RCS COMPUTED USING THE PWDI APPROACH ($\tilde{e}$) AND USING A HIGHLY ACCURATE SINGULAR INTEGRATION METHOD ($\hat{e}$)

h ($\times 10$)	4.34	3.62	3.12	2.72	1.98	1.37	1.05
e (%)	0.11	0.10	0.09	0.07	0.07	0.04	0.03
$\overline{e}$ (%)	0.65	0.47	0.64	0.34	0.29	0.18	0.20
$\tilde{e}$ (%)	10.2	7.56	7.05	4.38	3.25	1.24	0.72
$\hat{e}$ (%)	10.2	7.39	6.93	4.28	3.22	1.23	0.71

to numerically evaluate the resulting SS-regularized 4-D Galerkin-BEM integrals associated with the singular element interactions. Fig. 6 shows both the CPU times required to form the impedance matrices together with the relative monostatic-RCS errors (measured with respect to the exact value σ obtained from the Mie series solution) for each of the methods considered.

Next, in order to establish the actual accuracy with which singular integrals are computed using the PWDI method, we compare, for the same spherical meshes, the diagonal elements in the impedance matrix Z produced by the PWDI method, with the corresponding entries of the matrix Z^{ref} produced by the SS technique using a 1296-point Gauss quadrature rule. Nonsingular integrals in Z^{ref} are, on the other hand, computed using a six-point Gauss quadrature rule for triangles. We note that the latter matrix entries can be assumed to be exact since their integration errors are comparable to machine precision. Table II shows the relative errors: $e = \max_{1\le n\le N} |(Z)_{n,n} - (Z^{\text{ref}})_{n,n}| / \max_{1\le n\le N} |(Z^{\text{ref}})_{n,n}|$, $\overline{e} = \max_{1\le n\le N} |I_n - I_n^{\text{ref}}| / \max_{1\le n\le N} |I_n^{\text{ref}}|$, $\tilde{e} = |\tilde{\sigma} - \sigma|/\sigma$, and $\hat{e} = |\hat{\sigma} - \sigma|/\sigma$, in the diagonal of the PWDI-matrix, PWDI-computed currents (I_n), PWDI-computed monostatic RCS ($\tilde{\sigma}$), and SS-computed monostatic RCS using the aforementioned 1296-point Gauss quadrature rule ($\hat{\sigma}$), respectively, for various mesh sizes $h > 0$. The results presented in Fig. 6 and Table II demonstrate the competitiveness of the PWDI method in terms of both accuracy and efficiency. In particular, we observe from the results in Table II that the proposed PWDI regularization using a simple and inexpensive second-order three-point Gauss quadrature rule yields more than three digits of accuracy in evaluating the singular EFIE integrals, which results in a slightly smaller level of accuracy in the solution of the full linear system. We verified that the accuracy of this proposed PWDI method matches that of the SS approach using an 81-point quadrature while requiring less than half the time to compute in some cases considered. Furthermore, these results indicate that the solution accuracy is limited fundamentally by the planar triangular geometric modeling of the surface and the classical low-order RWG basis expansion functions utilized.

D. Other Examples

This section is devoted to demonstrate the capabilities of the proposed PWDI methodology at dealing with scattering by more realistic structures, for which the multiple-scattering EFIE formulation can be remarkably advantageous. It includes two example problems corresponding to a multiscale city-like PEC structure and another PEC structure whose complex shape is identical to that of the Anacleto Angelini Innovation Center Building at PUC's San Joaquín campus in Santiago, designed by the Pritzker prize winner architect, Alejandro Aravena.

1) Multiscale Object: We start off by considering a city-like PEC structure featuring six small-scale building-like struc-

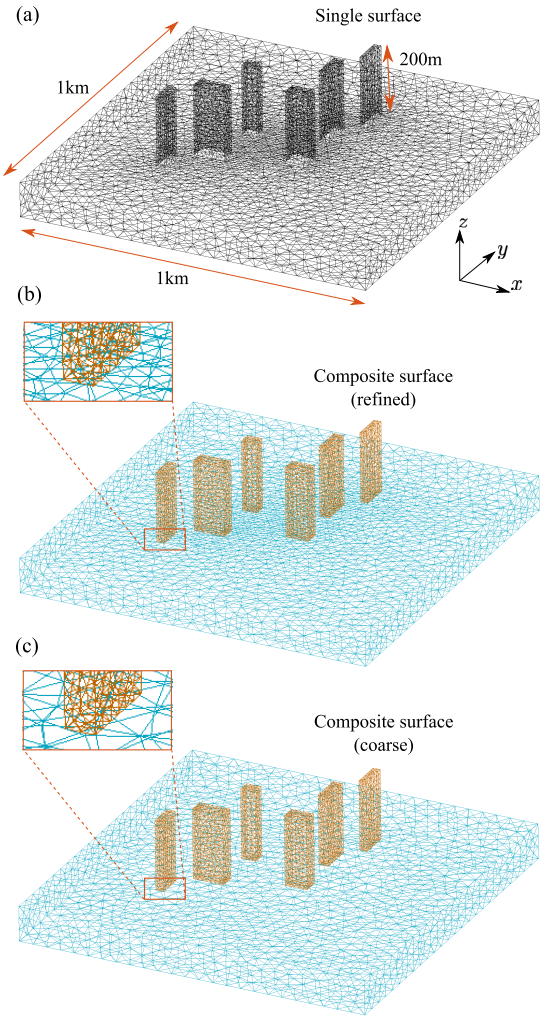

Fig. 7. (a) Mesh of a single surface representation of a city-like multiscale structure. (b) and (c) Nonconformal meshes of the two-part structure; the small-scale building-like blocks (depicted in orange) and the large-scale ground-like structure (depicted in light blue). The ground mesh displayed in (a) is locally refined around the base of the building so as to match the mesh size of the small-scale structures.

tures, which are shown in Fig. 7. The composite surface EFIE formulation enables in the case the solution of the problem using separate nonconformal meshes for the ground structure and for each one of the buildings, with mesh sizes adjusted according to the individual subdomain scales. This approach has in principle three main advantages over the standard single-surface EFIE formulation. First, it significantly reduces the overall number of degrees of freedom (and, consequently, reduce the size of the system matrix), if no local refinement of the large-scale surface is used around the edges at the base of the smaller scale subdomains (buildings). Second, it significantly simplifies the mesh processing of the geometry, as small-scale subdomains can be meshed separately and then be placed wherever is needed on the large-scale surface. Third, the technique can be attractive for repetitive modeling and simulation, as it allows to effectively separate geometrical details of interest from the rest of the geometry of the problem. Consequently, the diagonal blocks of the system matrix, corresponding to self-interactions of the composite surface parts, do not need to be recomputed when the individual surface parts undertake a rigid (Euclidian) transformation.

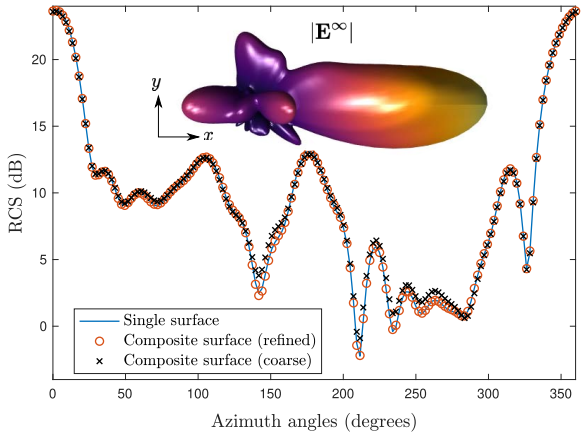

Fig. 8. Bistatic RCSs corresponding the solution of the problem of scattering of a planewave from the city-like PEC structure shown in Fig. 7, at zero elevation angle. Inset: corresponding view of the 3-D far-field pattern.

We solve here the problem of scattering of a planewave $\mathbf{E}^{\text{inc}}(\boldsymbol{r}) = (\boldsymbol{p} \times \boldsymbol{d})\,\mathrm{e}^{ik\boldsymbol{d}\cdot\boldsymbol{r}}$ with $f \approx 0.6$ MHz ($k = 2\pi/500$ rad/m and $\lambda = 500$ m), $\boldsymbol{d} = (4, 0, -1)/\sqrt{17}$, and $\boldsymbol{p} = (1, 1, 1)$, using both the standard and the multiple-scattering EFIE formulations. The algebraic PWDI kernel-regularization procedure with orders $M_1 = M_2 = 3$ was used in the numerical discretization of the two formulations; almost identical results are obtained using the analytical PWDI procedure. Two different meshes for the ground structure are utilized, a refined mesh around the base of the buildings, shown in Fig. 7(b), and a coarse mesh, irrespective of the presence of the buildings, which is shown in Fig. 7(c). The standard EFIE formulation, on the other hand, is discretized using the (conforming) mesh shown in Fig. 7(a).

The bistatic RCSs (at zero elevation) resulting from the solution of each one of the problems comprised in this example are presented in Fig. 8. The corresponding 3-D far-field pattern $\mathbf{E}^{\infty}(\hat{\boldsymbol{r}}) = 4\pi \lim_{|\boldsymbol{r}|\to\infty} |\boldsymbol{r}|^2 \mathbf{E}^{s}(\boldsymbol{r})$, with $\hat{\boldsymbol{r}} = \boldsymbol{r}/|\boldsymbol{r}|$, is shown in the inset of Fig. 8. As can be observed in this figure, a good agreement among the three RCSs is achieved, though slightly more accurate results are obtained using the locally refined mesh of the ground structure, especially around the 250° and 0° azimuth and elevation angles, respectively. Given the scale differences, the resulting surface currents around the base of buildings might not be well resolved when the coarse ground mesh is used, and this ends up introducing errors that are mitigated using local refinement. It is worth mentioning that although slightly less accurate, the size of the linear system matrix resulting from using the coarse mesh ($12\,354 \times 12\,354$) is remarkably smaller than the ones resulting from the locally refined mesh ($15\,744 \times 15\,744$) and the single (conforming) mesh ($17\,415 \times 17\,415$).

We now look into the issue of whether the impedance matrices resulting from the MoM discretization of the multiple-scattering EFIE formulation on composite surfaces have spectral properties and condition numbers similar to those resulting from the EFIE formulation on a single surface when applied to the same problem. In order to address this question, which is relevant for the design of effective preconditioners [43]–[47] for the solution of the linear system (9) using accelerated iterative solvers [48]–[52], we present Fig. 9(a),

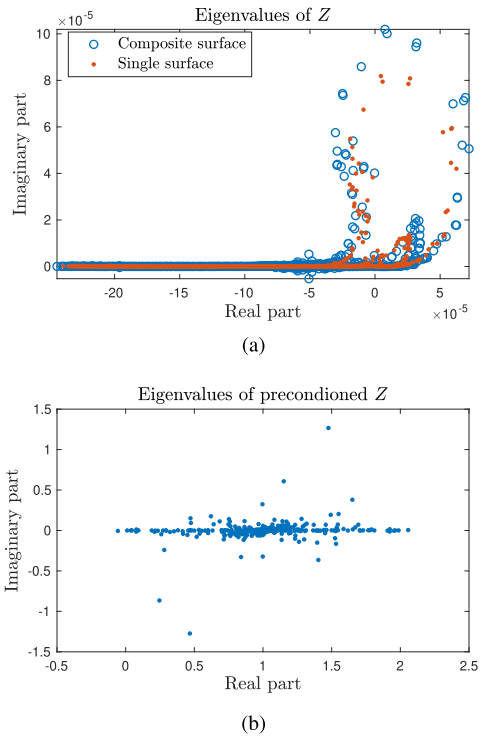

Fig. 9. (a) Eigenvalues of the impedance matrices corresponding to the composite- and single-surface EFIE formulations for the geometry shown in Fig. 7. (b) Eigenvalues of preconditioned impedance matrix corresponding to the composite surface.

which displays the eigenvalues of the impedance matrices Z, corresponding to the single and composite surface representation of the citylike structure in Fig. 7. As can be seen in Fig. 9(a), similar eigenvalue clustering patterns are observed for the two surface representations, with eigenvalues accumulating on the real axis and around the origin. This suggests that Calderón-type preconditioners should in principle improve the convergence of Krylov subspace linear algebra solvers when applied to matrices associated with the multiple-scattering EFIE formulation used on composite surfaces. The matrix condition number in the infinity (resp. one) norm, on the other hand, which amounts to $\kappa_\infty(Z) \approx 362$ (resp. $\kappa_1(Z) \approx 307$) for the composite surface and to $\kappa_\infty(Z) \approx 235$ (resp. $\kappa_1(Z) \approx 425$) for the single surface, is similar in this example. However, larger condition numbers are in general obtained for composite surface representations. A natural preconditioner for the multiple-scattering EFIE formulation is the block-diagonal proconditioner resulting from directly inverting the matrix blocks corresponding to the closed-surface components of the composite surface. We assess the effectiveness of this preconditioner in this example problem by applying GMRES [53] directly to the linear system resulting from the EFIE formulation applied on the single-surface and to the preconditioned system corresponding to the multiple-scattering EFIE formulation applied on the composite surface. For a tolerance of 10^{-4}, GMRES required 982 iterations in the single-surface case and just 33 iterations in the preconditioned composite-surface case. The eigenvalues of the preconditioned system are shown in Fig. 9(b). The effective and efficient preconditioning of impedance matrices resulting from the multiple-scattering

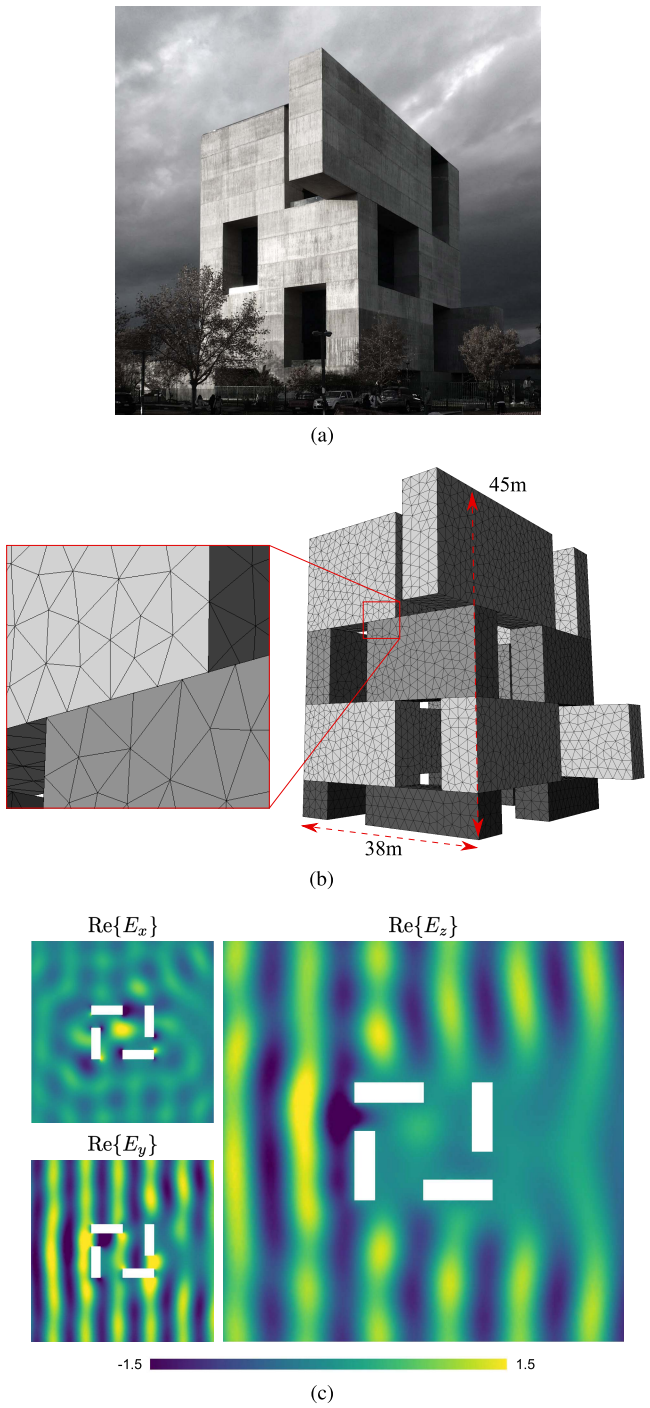

Fig. 10. Example of an actual structure whose surface can be easily modeled using a composite nonconforming surface mesh consisting of 16 rectangular blocks. (a) Innovation Center building at PUC, Chile. Credit: ELEMENTAL (Nina Vidic). (b) Composite-surface model of the Innovation Center building using nonconforming meshes. Each one of the 16 rectangular blocks making up its intricate facade was meshed separately using Gmsh software [40]. (c) Real part of the total electric field on the middle cross section ($z = 22.5$ m) of the building.

EFIE formulation on composite surfaces is a matter of ongoing research.

2) Innovation Center Building: This example considers the intricate geometry of the building shown in Fig. 10(a) whose facade consists of 16 rectangular blocks of various sizes. The problem of scattering of the planewave $\mathbf{E}^{\text{inc}}(\boldsymbol{r}) = (\boldsymbol{p}\times\boldsymbol{d})\,\mathrm{e}^{ik\boldsymbol{d}\cdot\boldsymbol{r}}$,

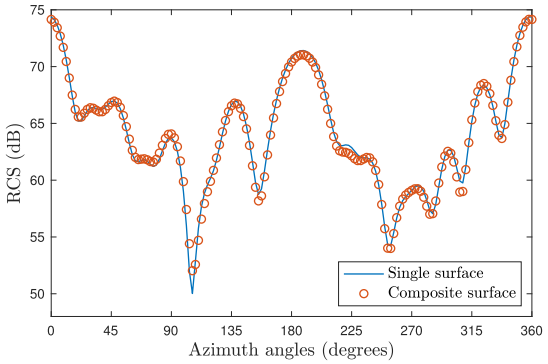

Fig. 11. Bistatic RCSs corresponding to the scattering of a planewave from the building shown in Fig. 10 at zero elevation angle.

with $f \approx 17.8$ MHz ($k = (2\pi/\lambda)$, $\lambda = 19$ m), $\boldsymbol{d} = (4, 0, -1)/\sqrt{17}$ and $\boldsymbol{p} = (1, 1, 1)$, from this structure is here solved by means of both the composite- and the standard-EFIE formulations using the MoM with PWDI kernel-regularized operators and RWG basis functions. The overall size of the composite nonconforming (resp. single conforming) mesh is $h = 2.34$ m (resp. $h = 2.49$ m), which leads to a $16\,206 \times 16\,206$ (resp. $16\,203 \times 16\,203$) linear systems matrix. The seemingly complex composite nonconforming mesh shown in Fig. 10(b) was rendered utilizing Gmsh software [40] (http://gmsh.info), which enables the mesh to be created by simply scaling, rotating, and translating a cube. The associated single conforming mesh was produced, on the other hand, by carefully and painstakingly defining the (non-Lipschitz) closed surface of the whole structure, also using Gmsh. Fig. 10(c) shows the real part of the three Cartesian components of the total electric field $\mathbf{E} = \mathbf{E}^s + \mathbf{E}^{\text{inc}}$ on the horizontal plane intersecting the building at 22.5 m height, which was evaluated by means of the kernel-regularized off-surface EFIE operator using the high-order algebraic PWDI with orders $M_1 = M_2 = 3$. The accuracy of this near-field calculation can be appraised in detail in the plot of the real part of E_z where it can be seen that the numerically generated E_z remains smooth at and around the surface and, furthermore, it vanishes exactly on the surface, as is it supposed to do in view of the PEC boundary condition (2). [A similar observation can be made about Fig. 5(a).] The resulting bistatic RCSs obtained using the two formulations are shown in Fig. 11 for the azimuth angles at zero elevation angle. Excellent agreement of the two solutions is obtained for this challenging geometric setup.

E. Switched Parasitic Antenna on a Finite Ground Plane

The final example of this article considers the switched parasitic antenna proposed in [54], which is shown in Fig. 12(a). The antenna is comprised of a small circular finite ground plane with a conductive sleeve, a center monopole feed element attached to the ground, four parasitic reflector elements also attached to the ground and uniformly distributed along its edge, and a fifth parasitic element isolated from the ground plane. The latter corresponds to the switch element that allows steering the radiation along the azimuth in its direction. The precise spatial dimensions of the antenna, which are provided

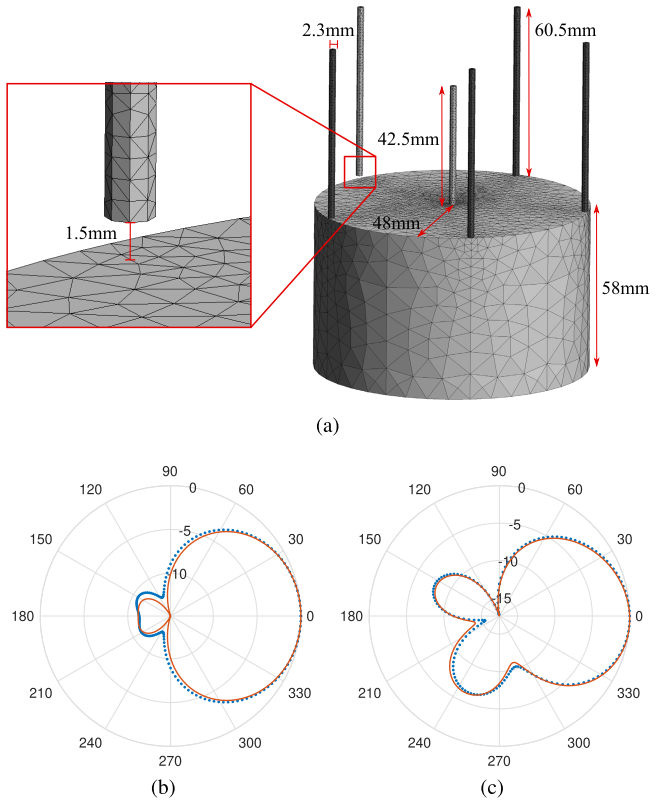

Fig. 12. (a) Composite surface mesh of the switched parasitic antenna proposed in [54]. Normalized radiation patterns for (b) azimuth and (c) elevation angles computed using the PWDI method (dotted lines). The solid lines correspond to reference radiation patterns computed using significantly refined conforming meshes.

in [54, Table II], were optimized in order to depress the main lobe elevation. In order to simulate the antenna using the multiple-scattering EFIE formulation (11), the delta gap model [38] is adopted to represent the monopole feed element. As indicated in [54, Fig. 2], on the other hand, the switch element is realized by simply raising it 1.5 mm above the ground plane [see Fig. 12(a)]. The antenna is represented in this example as a composite surface mesh comprising six closed-surface meshes corresponding to the skirted finite ground plane with the feed element attached and the five parasitic cylindrical elements. The actual meshes used in the calculations are shown in Fig. 12(a). The EFIE is then numerically solved by means of the proposed PWDI technique. Only two meshes are needed to form the impedance matrix Z, as by design the five parasitic elements are identical. This allows Z (of size $14\,793 \times 14\,793$) to be efficiently computed by taking advantage of the fact that the diagonal blocks corresponding to the parasitic elements are also identical in this case. The resulting antenna radiation patterns at the operation frequency 1.575 GHz are shown in Fig. 12(b) and (c), along with reference radiation patterns computed using two significantly refined conforming meshes corresponding to the switch element and the rest of the antenna (the impedance matrix associated with the reference solution has size $20\,103 \times 20\,103$). Note that excellent agreement with both the experimental and the finite-element-produced radiation patterns shown in [54, Fig. 4] is achieved.

VIII. Conclusion

This article extended the PWDI methodology put forth in [23] and [24] to the classical EFIE formulation for scattering from closed PEC surfaces. We show that the PWDI methodology enables the direct evaluation of Galerkin-MoM impedance matrices using standard quadrature rules, thus significantly simplifying the practical implementation of the MoM. The ability of our method to simultaneously evaluate accurately singular and nearly singular integrals regardless of the singularity location allowed us to introduce a novel EFIE formulation based on nonoverlapping subdomain partitioning and use of composite surface representations. This new formulation has the capability of simplifying the geometric treatment of complex 3-D structures by enabling the use of nonconforming surface meshes. The advantages of this formulation were demonstrated by applying it to a multiscale structure and an intricate (non-Lipschitz) surface modeling an actual building facade.

The proposed methodology opens up multiple future research directions. We first mention the immediate extensions/modifications of the PWDI technique to the magnetic-field integral equation (MFIE) formulation for PEC scattering problems and to the Poggio–Miller–Chang–Harrington–Wu–Tsai (PMCHWT) [55] and Müller [56] formulations for electromagnetic transmission problems. Yet, another research direction has to do with the extension of the proposed PWDI methodology to problems involving unbounded (nonperiodic) material interfaces, such as half-spaces, layered media, and waveguides. Current research efforts by the authors in this direction include combining the PWDI technique with the windowed Green function method for frequency [57]–[59] and time-domain [60] scattering problems, so as to produce a general-purpose robust and efficient integral equation solver based solely on the free-space Helmholtz Green function.

References

[1] S. Rao, D. Wilton, and A. Glisson, "Electromagnetic scattering by surfaces of arbitrary shape," *IEEE Trans. Antennas Propag.*, vol. AP-30, no. 3, pp. 409–418, May 1982.

[2] A. Tzoulis and T. F. Eibert, "Review of singular potential integrals for method of moments solutions of surface integral equations," *Adv. Radio Sci.*, vol. 2, no. B2, pp. 93–99, May 2005.

[3] D. Wilton, S. Rao, A. Glisson, D. Schaubert, O. Al-Bundak, and C. Butler, "Potential integrals for uniform and linear source distributions on polygonal and polyhedral domains," *IEEE Trans. Antennas Propag.*, vol. AP-32, no. 3, pp. 276–281, Mar. 1984.

[4] R. D. Graglia, "On the numerical integration of the linear shape functions times the 3-D Green's function or its gradient on a plane triangle," *IEEE Trans. Antennas Propag.*, vol. 41, no. 10, pp. 1448–1455, Oct. 1993.

[5] S. Caorsi, D. Moreno, and F. Sidoti, "Theoretical and numerical treatment of surface integrals involving the free-space Green's function," *IEEE Trans. Antennas Propag.*, vol. 41, no. 9, pp. 1296–1301, Sep. 1993.

[6] P. Yla-Oijala and M. Taskinen, "Calculation of cfie impedance matrix elements with RWG and n×RWG functions," *IEEE Trans. Antennas Propag.*, vol. 51, no. 8, pp. 1837–1846, Aug. 2003.

[7] S. A. Sauter, "Cubature Techniques for 3-D Galerkin BEM," in *Boundary Elements: Implementation and Analysis of Advanced Algorithms*. Wiesbaden, Germany: Vieweg+Teubner Verlag, 1996, pp. 29–44.

[8] C. Schwab and W. L. Wendland, "On numerical cubatures of singular surface integrals in boundary element methods," *Numerische Math.*, vol. 62, no. 1, pp. 343–369, Dec. 1992.

[9] M. T. H. Reid, J. K. White, and S. G. Johnson, "Generalized Taylor–Duffy method for efficient evaluation of Galerkin integrals in boundary-element method computations," *IEEE Trans. Antennas Propag.*, vol. 63, no. 1, pp. 195–209, Jan. 2015.

[10] D. J. Taylor, "Accurate and efficient numerical integration of weakly singular integrals in Galerkin EFIE solutions," *IEEE Trans. Antennas Propag.*, vol. 51, no. 7, pp. 1630–1637, Jul. 2003.

[11] A. G. Polimeridis and J. R. Mosig, "Complete semi-analytical treatment of weakly singular integrals on planar triangles via the direct evaluation method," *Int. J. Numer. Methods Eng.*, vol. 83, no. 12, pp. 1625–1650, Sep. 2010.

[12] M. G. Duffy, "Quadrature over a pyramid or cube of integrands with a singularity at a vertex," *SIAM J. Numer. Anal.*, vol. 19, no. 6, pp. 1260–1262, Dec. 1982.

[13] W. Hackbusch and S. A. Sauter, "On numerical cubatures of nearly singular surface integrals arising in BEM collocation," *Computing*, vol. 52, no. 2, pp. 139–159, Jun. 1994.

[14] D. Tihon and C. Craeye, "All-analytical evaluation of the singular integrals involved in the method of moments," *IEEE Trans. Antennas Propag.*, vol. 66, no. 4, pp. 1925–1936, Apr. 2018.

[15] M. M. Botha, "A family of augmented duffy transformations for near-singularity cancellation quadrature," *IEEE Trans. Antennas Propag.*, vol. 61, no. 6, pp. 3123–3134, Jun. 2013.

[16] M. M. Botha, "Numerical integration scheme for the near-singular green function gradient on general triangles," *IEEE Trans. Antennas Propag.*, vol. 63, no. 10, pp. 4435–4445, Oct. 2015.

[17] M. A. Khayat, D. R. Wilton, and P. W. Fink, "An improved transformation and optimized sampling scheme for the numerical evaluation of singular and near-singular potentials," *IEEE Antennas Wireless Propag. Lett.*, vol. 7, pp. 377–380, 2008.

[18] M. A. Khayat and D. R. Wilton, "Numerical evaluation of singular and near-singular potential integrals," *IEEE Trans. Antennas Propag.*, vol. 53, no. 10, pp. 3180–3190, Oct. 2005.

[19] J. C. F. Telles, "A self-adaptive co-ordinate transformation for efficient numerical evaluation of general boundary element integrals," *Int. J. Numer. Methods Eng.*, vol. 24, no. 5, pp. 959–973, May 1987.

[20] K. Hayami and H. Matsumoto, "A numerical quadrature for nearly singular boundary element integrals," *Eng. Anal. Boundary Elements*, vol. 13, no. 2, pp. 143–154, Jan. 1994.

[21] L. Scuderi, "On the computation of nearly singular integrals in 3D BEM collocation," *Int. J. Numer. Methods Eng.*, vol. 74, no. 11, pp. 1733–1770, Jun. 2008.

[22] F. Vipiana and D. R. Wilton, "Numerical evaluation via singularity cancellation schemes of near-singular integrals involving the gradient of Helmholtz-type potentials," *IEEE Trans. Antennas Propag.*, vol. 61, no. 3, pp. 1255–1265, Mar. 2013.

[23] C. Pérez-Arancibia, "A plane-wave singularity subtraction technique for the classical Dirichlet and neumann combined field integral equations," *Appl. Numer. Math.*, vol. 123, pp. 221–240, Jan. 2018.

[24] C. Pérez-Arancibia, C. Turc, and L. Faria, "Planewave density interpolation methods for 3D Helmholtz boundary integral equations," *SIAM J. Sci. Comput.*, vol. 41, no. 4, pp. A2088–A2116, 2019.

[25] C. Pérez-Arancibia, L. M. Faria, and C. Turc, "Harmonic density interpolation methods for high-order evaluation of laplace layer potentials in 2D and 3D," *J. Comput. Phys.*, vol. 376, pp. 411–434, Jan. 2019.

[26] R. N. Simpson, Z. Liu, R. Vázquez, and J. A. Evans, "An isogeometric boundary element method for electromagnetic scattering with compatible B-spline discretizations," *J. Comput. Phys.*, vol. 362, pp. 264–289, Jun. 2018.

[27] W. Cai, T. Yu, H. Wang, and Y. Yu, "High-order mixed RWG basis functions for electromagnetic applications," *IEEE Trans. Microw. Theory Techn.*, vol. 49, no. 7, pp. 1295–1303, Jul. 2001.

[28] W. Cai, Y. Yu, and X. C. Yuan, "Singularity treatment and high-order RWG basis functions for integral equations of electromagnetic scattering," *Int. J. Numer. Methods Eng.*, vol. 53, no. 1, pp. 31–47, Jan. 2002.

[29] O. Bruno, T. Elling, R. Paffenroth, and C. Turc, "Electromagnetic integral equations requiring small numbers of Krylov-subspace iterations," *J. Comput. Phys.*, vol. 228, no. 17, pp. 6169–6183, Sep. 2009.

[30] D. S. Weile and E. Michielssen, "Genetic algorithm optimization applied to electromagnetics: A review," *IEEE Trans. Antennas Propag.*, vol. 45, no. 3, pp. 343–353, Mar. 1997.

[31] G. F. Uler, O. A. Mohammed, and C.-S. Koh, "Utilizing genetic algorithms for the optimal design of electromagnetic devices," *IEEE Trans. Magn.*, vol. 30, no. 6, pp. 4296–4298, Nov. 1994.

[32] E. Jorgensen, P. Meincke, and O. Breinbjerg, "An efficient fringe integral equation method for optimizing the antenna location on complex bodies," in *Proc. IEEE Antennas Propag. Soc. Int. Symp. Dig. Held Conjunct USNC/URSI Nat. Radio Sci. Meeting*, Jul. 2001, pp. 584–587.
[33] E. M. Koper, W. D. Wood, and S. W. Schneider, "Aircraft antenna coupling minimization using genetic algorithms and approximations," *IEEE Trans. Aerosp. Electron. Syst.*, vol. 40, no. 2, pp. 742–751, Apr. 2004.
[34] Z. Peng, X.-C. Wang, and J.-F. Lee, "Integral equation based domain decomposition method for solving electromagnetic wave scattering from non-penetrable objects," *IEEE Trans. Antennas Propag.*, vol. 59, no. 9, pp. 3328–3338, Sep. 2011.
[35] Z. Peng, R. Hiptmair, Y. Shao, and B. MacKie-Mason, "Domain decomposition preconditioning for surface integral equations in solving challenging electromagnetic scattering problems," *IEEE Trans. Antennas Propag.*, vol. 64, no. 1, pp. 210–223, Jan. 2016.
[36] M. A. Echeverri Bautista, F. Vipiana, M. A. Francavilla, J. A. Tobon Vasquez, and G. Vecchi, "A nonconformal domain decomposition scheme for the analysis of multiscale structures," *IEEE Trans. Antennas Propag.*, vol. 63, no. 8, pp. 3548–3560, Aug. 2015.
[37] D. L. Colton and R. Kress, *Integral Equation Methods Scattering Theory* (Pure and Applied Mathematics). 1st ed. Hoboken, NJ, USA: Wiley, 1983.
[38] J. Volakis, *Integral Equation Methods for Electromagnetics*. Rijeka, Croatia: SciTech, 2012.
[39] G. R. Cowper, "Gaussian quadrature formulas for triangles," *Int. J. Numer. Methods Eng.*, vol. 7, no. 3, pp. 405–408, 1973.
[40] C. Geuzaine and J.-F. Remacle, "Gmsh: A 3-D finite element mesh generator with built-in pre- and post-processing facilities," *Int. J. Numer. Methods Eng.*, vol. 79, no. 11, pp. 1309–1331, Sep. 2009.
[41] S. A. Sauter and C. Schwab, *Boundary Element Methods*. Berlin, Germany: Springer, 2010.
[42] C. A. Balanis, *Advanced Engineering Electromagnetics*, 2nd ed. Hoboken, NJ, USA: Wiley, 2012.
[43] F. P. Andriulli *et al.*, "A multiplicative calderon preconditioner for the electric field integral equation," *IEEE Trans. Antennas Propag.*, vol. 56, no. 8, pp. 2398–2412, Aug. 2008.
[44] R. J. Adams, "Physical and analytical properties of a stabilized electric field integral equation," *IEEE Trans. Antennas Propag.*, vol. 52, no. 2, pp. 362–372, Feb. 2004.
[45] H. Contopanagos *et al.*, "Well-conditioned boundary integral equations for three-dimensional electromagnetic scattering," *IEEE Trans. Antennas Propag.*, vol. 50, no. 12, pp. 1824–1830, Dec. 2002.
[46] S. Borel, D. P. Levadoux, and F. Alouges, "A new well-conditioned integral formulation for Maxwell equations in three dimensions," *IEEE Trans. Antennas Propag.*, vol. 53, no. 9, pp. 2995–3004, Sep. 2005.
[47] M. B. Stephanson and J.-F. Lee, "Preconditioned electric field integral equation using calderon identities and dual loop/star basis functions," *IEEE Trans. Antennas Propag.*, vol. 57, no. 4, pp. 1274–1279, Apr. 2009.
[48] J. Song, C.-C. Lu, and W. C. Chew, "Multilevel fast multipole algorithm for electromagnetic scattering by large complex objects," *IEEE Trans. Antennas Propag.*, vol. 45, no. 10, pp. 1488–1493, Oct. 1997.
[49] J. M. Song and W. C. Chew, "Multilevel fast-multipole algorithm for solving combined field integral equations of electromagnetic scattering," *Microw. Opt. Technol. Lett.*, vol. 10, no. 1, pp. 14–19, Sep. 1995.
[50] W. C. Chew, E. Michielssen, J. Song, and J.-M. Jin, *Fast and Efficient Algorithms in Computational Electromagnetics*. Norwood, MA, USA: Artech House, 2001.
[51] W. Cho Chew, J.-M. Jin, C.-C. Lu, E. Michielssen, and J. M. Song, "Fast solution methods in electromagnetics," *IEEE Trans. Antennas Propag.*, vol. 45, no. 3, pp. 533–543, Mar. 1997.
[52] S. Mo Seo and J.-F. Lee, "A fast IE-FFT algorithm for solving PEC scattering problems," *IEEE Trans. Magn.*, vol. 41, no. 5, pp. 1476–1479, May 2005.
[53] Y. Saad and M. H. Schultz, "GMRES: A generalized minimal residual algorithm for solving nonsymmetric linear systems," *SIAM J. Sci. Stat. Comput.*, vol. 7, no. 3, pp. 856–869, Jul. 1986.
[54] R. Schlub and D. V. Thiel, "Switched parasitic antenna on a finite ground plane with conductive sleeve," *IEEE Trans. Antennas Propag.*, vol. 52, no. 5, pp. 1343–1347, May 2004.
[55] A. J. Poggio and E. K. Miller, "Integral equation solutions of three-dimensional scattering problems," in *Computer Techniques for Electromagnetics*, R. Mittra, Ed. New York, NY, USA: Pergamom Press, 1973, ch. 4.
[56] C. Müller, *Foundations of the Mathematical Theory of Electromagnetic Waves*, vol. 155. Berlin, Germany: Springer, 2013.
[57] O. P. Bruno, M. Lyon, C. Pérez-Arancibia, and C. Turc, "Windowed green function method for layered-media scattering," *SIAM J. Appl. Math.*, vol. 76, no. 5, pp. 1871–1898, Jan. 2016.
[58] O. P. Bruno and C. Pérez-Arancibia, "Windowed Green function method for the Helmholtz equation in the presence of multiply layered media," *Proc. Roy. Soc. London, Ser. A*, vol. 473, no. 2202, pp. 1–20, 2017.
[59] O. P. Bruno, E. Garza, and C. Pérez-Arancibia, "Windowed green function method for nonuniform open-waveguide problems," *IEEE Trans. Antennas Propag.*, vol. 65, no. 9, pp. 4684–4692, Sep. 2017.
[60] I. Labarca, L. M. Faria, and C. Pérez-Arancibia, "Convolution quadrature methods for time-domain scattering from unbounded penetrable interfaces," *Proc. Roy. Soc. London, Ser. A*, vol. 475, no. 2227, pp. 1–18, 2019.

Carlos Pérez-Arancibia (Member, IEEE) received the B.S. and M.S. degrees in engineering sciences from Pontificia Universidad Católica (PUC), Santiago, Chile, in 2008 and 2010, respectively, and the Ph.D. degree in applied computational mathematics from Caltech, Pasadena, CA, USA, in 2016.

He was an Instructor in Applied Mathematics at MIT, Cambridge, MA, USA, from 2016 to 2018. Since 2018, he has been an Assistant Professor with the Institute for Mathematical and Computational Engineering, PUC. His research interests lie at the intersection of scientific computing and wave phenomena.

Catalin Turc was born in Suceava, Romania, in 1975. He received the B.S. degree in mathematics from "A. I. Cuza" University, Iaşi, Romania, in 1997, and the Ph.D. degree in mathematics from the University of Minnesota, Minneapolis, MN, USA, in 2005.

He was a Post-Doctoral Scholar at Caltech, Pasadena, CA, USA, and then an Assistant Professor at UNC Charlotte, Charlotte, NC, USA, and Case Western Reserve University, Cleveland, OH, USA. Since 2012, he has been an Associate Professor with the Department of Mathematical Sciences, New Jersey Institute of Technology (NJIT), Newark, NJ, USA. His research interests are in scientific computing and numerical analysis.

Luiz M. Faria received the Ph.D. degree in applied mathematics and computational sciences from the King Abdullah University of Science and Technology, Thuwal, Saudi Arabia, in 2015, working on asymptotic models for combustion waves.

From 2015 to 2018, he was an Instructor in Applied Mathematics with MIT, Cambridge, MA, USA, where he worked on free surface waves and boundary integral equation methods. After a brief period working in the industry, he joined INRIA, Paris, France, in a Starting Research Position in 2019, working at the POEMS Laboratory, where he currently resides.

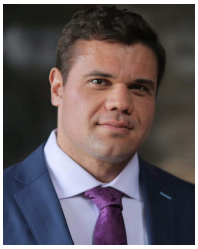

Constantine Sideris (Member, IEEE) received the B.S., M.S., and Ph.D. degrees (Hons.) from the California Institute of Technology (Caltech), Pasadena, CA, USA, in 2010, 2011, and 2017, respectively.

He was a Visiting Scholar at the UC Berkeley's Wireless Research Center, Berkeley, CA, USA, from 2013 to 2014. He was a Post-Doctoral Scholar with the Department of Computing and Mathematical Sciences, Caltech, from 2017 to 2018, working on integral equation methods for electromagnetics. He is currently an Assistant Professor of electrical and computer engineering with the University of Southern California, Los Angeles, CA, USA. His research interests include RF and millimeter-wave integrated circuits for bioelectronics and wireless communications, applied electromagnetics, and computational electromagnetics for antenna design and silicon photonics.

Dr. Sideris was a recipient of the AFOSR YIP Award in 2020, the Caltech Leadership Award in 2017, and the NSF Graduate Research Fellowship in 2010.